Vol 445|22 February 2007|doi:10.1038/nature05578

LETTERS

Moisture transport across Central America as a positive feedback on abrupt climatic changes

Guillaume Leduc[1], Laurence Vidal[1], Kazuyo Tachikawa[1], Frauke Rostek[1], Corinne Sonzogni[1], Luc Beaufort[1] & Edouard Bard[1]

Moisture transport from the Atlantic to the Pacific ocean across Central America leads to relatively high salinities in the North Atlantic Ocean[1] and contributes to the formation of North Atlantic Deep Water[2]. This deep water formation varied strongly between Dansgaard/Oeschger interstadials and Heinrich events—millennial-scale abrupt warm and cold events, respectively, during the last glacial period[3]. Increases in the moisture transport across Central America have been proposed to coincide with northerly shifts of the Intertropical Convergence Zone and with Dansgaard/Oeschger interstadials, with opposite changes for Heinrich events[4]. Here we reconstruct sea surface salinities in the eastern equatorial Pacific Ocean over the past 90,000 years by comparing palaeotemperature estimates from alkenones and Mg/Ca ratios with foraminiferal oxygen isotope ratios that vary with both temperature and salinity. We detect millennial-scale fluctuations of sea surface salinities in the eastern equatorial Pacific Ocean of up to two to four practical salinity units. High salinities are associated with the southward migration of the tropical Atlantic Intertropical Convergence Zone, coinciding with Heinrich events and with Greenland stadials[5]. The amplitudes of these salinity variations are significantly larger on the Pacific side of the Panama isthmus, as inferred from a comparison of our data with a palaeoclimate record from the Caribbean basin[6]. We conclude that millennial-scale fluctuations of moisture transport constitute an important feedback mechanism for abrupt climate changes, modulating the North Atlantic freshwater budget and hence North Atlantic Deep Water formation.

Paleotemperatures recorded in Greenland indicate that rapid climatic changes occurred on a millennial timescale during Marine Isotope Stage 3 (MIS3[5,7], between 59 and 25 kyr BP) and were intimately linked to the process of North Atlantic Deep Water (NADW) formation[2,3] (the Dansgaard–Oeschger[5] and Heinrich events[7], H-DO variability). The H-DO features are also observed in tropical areas sensitive to summer monsoon fluctuations, which were linked to latitudinal shifts of the Intertropical Convergence Zone (ITCZ)[4,8,9]. To explain the existence of H-DO features at different latitudes, we need to understand how climatic teleconnections are set up between high and low latitudes and/or different ocean basins[10,11].

In modern climatology, the interoceanic freshwater transfer from the Atlantic to the Pacific Oceans maintains the high Atlantic salinity required for NADW formation[1]. This is achieved by the combination of strong easterly winds and increased atmospheric humidity within the Caribbean region[12], which occurs mainly during the boreal summer when the ITCZ is shifted northward (Supplementary Information). Modelling studies imply that the modern interoceanic vapour flux ranges from 0.13 Sv (ref. 1) to 0.45 Sv (ref. 13) ($1\,Sv = 10^6\,m^3\,s^{-1}$).

For the Last Glacial Maximum (LGM), different models show either an increased[14] or a decreased[15] water vapour export from the Atlantic Ocean. Recent work on marine sequences covering the last deglaciation suggested that cross-isthmus vapour transport was not strongly affected by glacial boundary conditions[16]. Rather, the interoceanic vapour transport and the interbasin salt contrast seem to have been influenced by ITCZ dynamics, which contributed to the hydrological variability in the Eastern Equatorial Pacific (EEP) region[16]. From this point of view, the EEP appears to be a key climatic crossroad involved in rapid climatic changes. To understand better how the ITCZ dynamics and the moisture transfer changes across Central America evolved with respect to the H-DO variability, it is crucial to gather observations covering the entire MIS3, and in particular at the prominent six Heinrich events. Since the EEP sea surface salinities (SSS) are intimately linked to the intensity of the ITCZ and its mean latitudinal position (Fig. 1), reconstructing past EEP SSS fluctuations allows us to track variations in moisture transport across the Panama isthmus (Supplementary Information).

Here we present a multi-proxy record of past EEP hydrological characteristics from the sediment core MD02-2529 (08° 12.33′ N, 84° 07.32′ W, 1,619 m water depth) (Fig. 2). The $\delta^{18}O$ values for the surface-dwelling foraminifer *Globigerinoides ruber* ($\delta^{18}O_{G.\,ruber}$) are about −3‰ for the Holocene and decrease by about 2‰ between the MIS2 and the late Holocene (Fig. 2a). Rapid $\delta^{18}O_{G.\,ruber}$ variations of 0.5 to 1‰ occurred on a millennial timescale during MIS2 and the late part of MIS3. Two longer cycles with saw-tooth shapes are recorded between 40 and 46 kyr BP and between 46 and 53 kyr BP. From 58 to 90 kyr BP, fluctuations are observed with longer wavelengths and weaker amplitudes than the $\delta^{18}O_{G.\,ruber}$ shifts during MIS2 and 3.

The $U^{k'}_{37}$ sea surface temperatures ($U^{k'}_{37}$-SST) reconstruction agrees well with the record of the Mg/Ca-SST measured on *G. ruber*, except between 20 and 25 kyr BP (Fig. 2b, Supplementary Information). The mean Holocene SST of 28 °C (Fig. 2b) is within the range of modern SST values (Supplementary Information). A long-term 3 °C increase occurred between 25 and 10 kyr BP in $U^{k'}_{37}$-SST. The SST record for MIS3, 4 and 5 varies between 24.5 and 28 °C with minima and maxima centred at 30, 43 and 65 kyr BP, and at 38, 57 and 85 kyr BP, respectively. Therefore the EEP SST appear to vary independently from the millennial-scale variability of $\delta^{18}O_{G.\,ruber}$ (Fig. 2a, b), and the $\delta^{18}O$ of sea water ($\delta^{18}O_{sw}$) clearly indicates that the large-amplitude millennial-scale $\delta^{18}O_{G.\,ruber}$ fluctuations are driven by $\delta^{18}O_{sw}$ variations (Fig. 2a, c and Supplementary Information).

After the removal of the global $\delta^{18}O_{sw}$ linked to sea-level variations (ref. 17), rapid fluctuations in $\Delta\delta^{18}O_{sw}$ (a proxy for regional SSS) persist throughout the sequence (Fig. 3c). For the modern climate, a northern position of the ITCZ during the boreal summer leads to increased net precipitation in the EEP region (Fig. 1). Indeed, about half of the EEP precipitation originates from the Caribbean[18] and is brought to the Pacific side through zonal atmospheric transport

[1]CEREGE, UMR6635, CNRS Université Paul Cézanne Aix-Marseille III, Collège de France, Europôle de l'Arbois, BP 80, 13545 Aix-en-Provence Cedex 04, France.

across Central America, mainly during the wet summer season[12] (Supplementary Information). The salinity record based on $\Delta\delta^{18}O_{sw}$ can therefore be used as an indicator of rainfall and, in connection with similar records, of cross-isthmus moisture transport. Time intervals with low $\Delta\delta^{18}O_{sw}$ should correspond to periods of intensified moisture fluxes across the Panama isthmus.

The high-resolution reflectance record of the Cariaco Basin (Fig. 1) results from high/low productivity and terrigenous input associated with the northward/southward shifts of the ITCZ over the last glacial period[4]. The northern position of the ITCZ appears to be in phase with DO interstadials[4], while southward migrations of the ITCZ are in phase with Heinrich events and DO stadials (Fig. 3a, b). The MD02-2529 $\Delta\delta^{18}O_{sw}$ and Cariaco Basin reflectance data indicate that the northward migration of the ITCZ in the Cariaco Basin is associated with EEP SSS minima, and so to enhanced moisture export from the Atlantic, when the ITCZ was aligned with the Central America low-level mountain channels[4] (Fig. 3b, c). Therefore, the Equatorial Atlantic and the EEP are efficiently linked through atmospheric teleconnection.

Maximum EEP SSS occurred during H events and DO stadials (Fig. 3c). This is compatible with a southward migration of the ITCZ accompanied by a decrease in water vapour transport to the Pacific Ocean. The ITCZ displacements are also documented in northeastern Brazil at 10° S by well-dated growth phases of speleothems during the prominent H events, indicating wet climate at these periods[19] (Fig. 3d). The modern distribution of precipitation over South America in March (Fig. 1) implies a southward migration of the ITCZ over the Amazon Basin at the times of H events (Fig. 3d). These enhanced rainfall time intervals correspond to periods of increased runoff to the tropical Atlantic, as is clearly recorded in shallow sediments along the northeastern Brazilian coast[20] (Figs 1 and 3d). The orogenic blocking by the Andes prevented the export of water vapour from the Atlantic to the Pacific, and probably induced the recirculation of freshwater within the Atlantic Ocean during H events and DO stadials, mainly via the Amazon River outflow.

We consider similar records obtained from cores retrieved on the other side of the Panama isthmus in order to better constrain the EEP hydrological changes and to further study the moisture transport from the Atlantic to the Pacific. Recent work on a Caribbean sediment core (Fig. 1) has recorded regional SSS maxima during Heinrich events and the Younger Dryas[6], indicating that both sides of the isthmus were strongly influenced by north–south shifts of the ITCZ (Fig. 1), making the Atlantic and the Pacific salinity records in phase for their main features. However, a second-order antiphase pattern is superimposed on these first-order variations, and is linked to cross-isthmus moisture transport. Evidence for this second-order antiphase is seen when the respective amplitudes of salinity changes

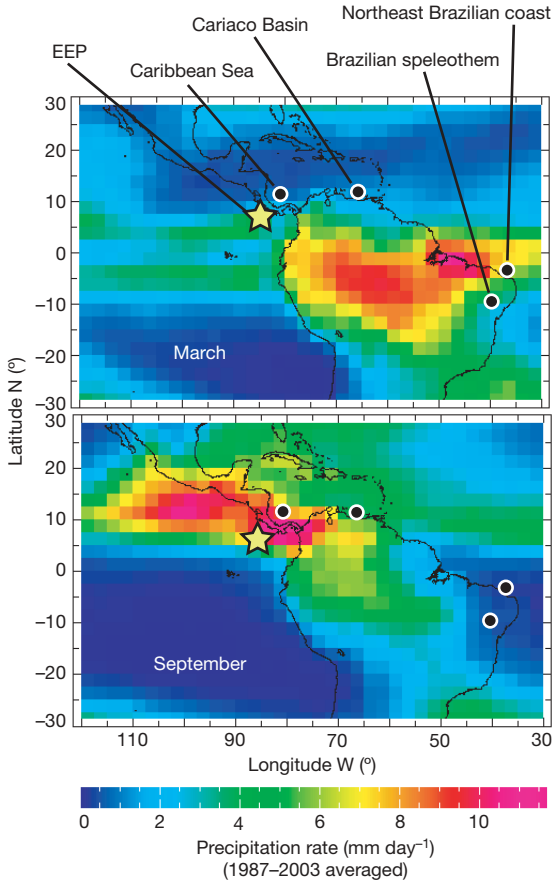

Figure 1 | Averaged precipitation rates over South America for March and September for the period AD 1987–2003. Black dots indicate locations of palaeoclimatic archives discussed in the text, that is, the comparison of the EEP (core MD02-2529, yellow star, this study) to the sedimentary sequences of the Cariaco Basin (ODP hole 1002C)[4], of the Caribbean Sea (core VM28-122 and ODP hole 999A)[6] and of the northeastern Brazilian margin (core GeoB3104-1/3912-1)[20] as well as the northeastern Brazil speleothem growing phases[19]. Rainfall data were retrieved from the International Research Institute for Climate Prediction and are available at http://iri.ldeo.columbia.edu.

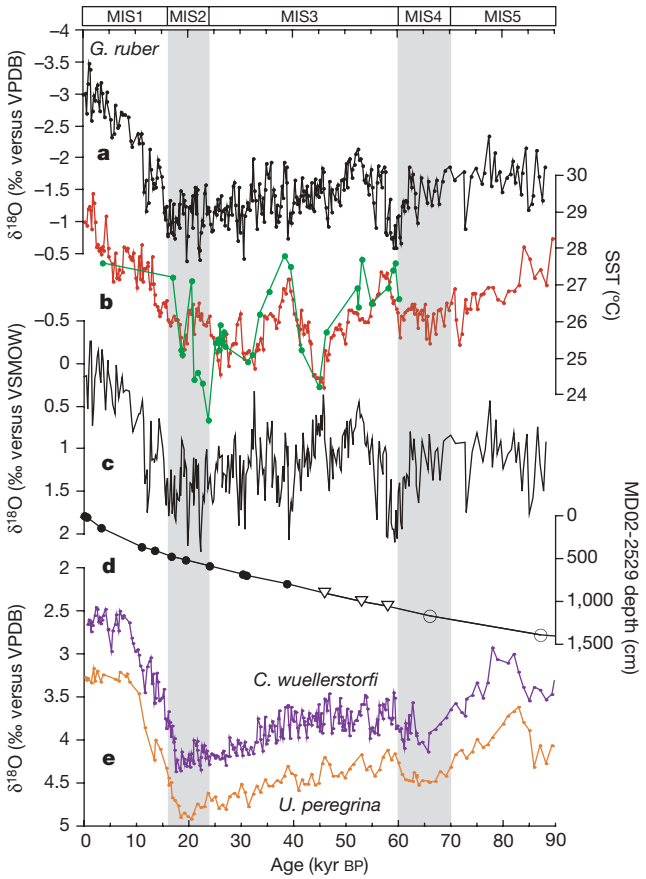

Figure 2 | Records of MD02-2529 versus age for the last 90 kyr BP. **a**, $\delta^{18}O$ record of the surface-dwelling planktonic foraminifer *G. ruber*. **b**, Comparison of $U^{K'}_{37}$-SST (red curve) and Mg/Ca-SST (green curve). **c**, Calculated $\delta^{18}O_{sw}$. **d**, Age–depth relationship based on radiocarbon measurements (black dots) and benthic foraminifera stratigraphy tuned to Byrd (open triangles) and to a benthic $\delta^{18}O$ stack (open circles) (see Supplementary Information for the age model construction). **e**, $\delta^{18}O$ records of the benthic species *Cibicidoides wuellerstorfi* (blue curve) and *Uvigerina peregrina* (orange curve). VPDB, Vienna Pee-Dee Belemnite standard; VSMOW, Vienna Standard Mean Ocean Water.

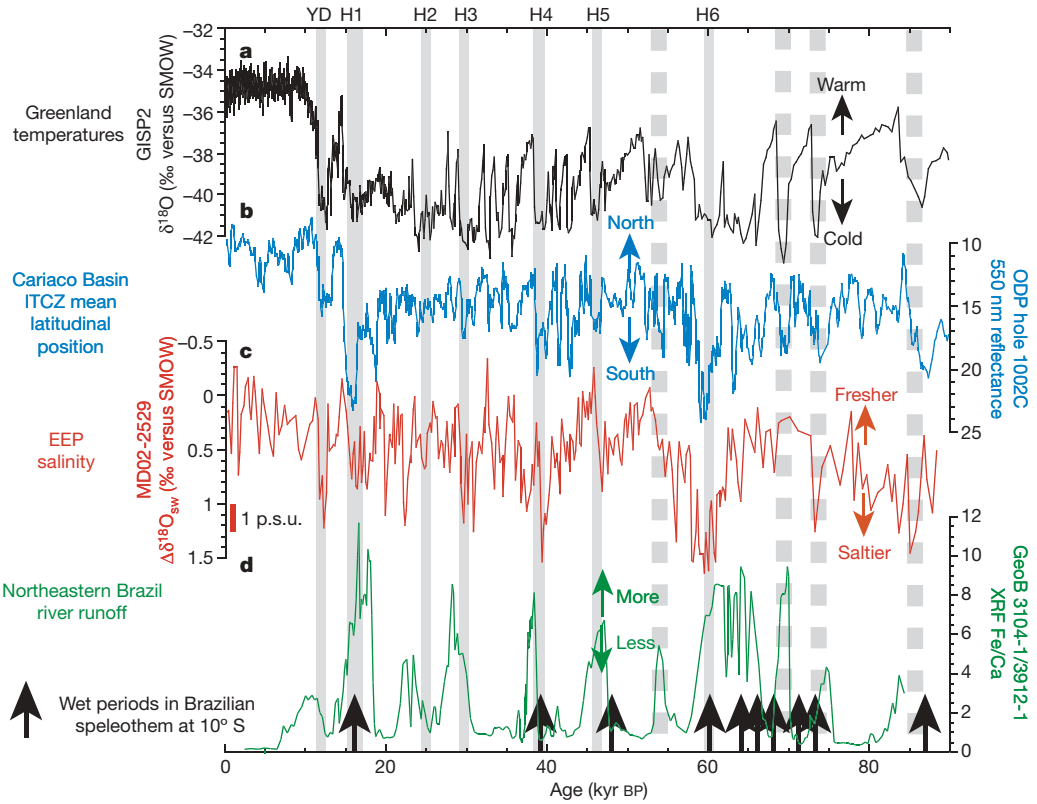

Figure 3 | Temporal variations of the calculated $\Delta\delta^{18}O_{sw}$ of MD02-2529 compared to other palaeoclimatic records. The data are presented on their published original timescales without further tuning. **a**, Greenland GISP2 palaeotemperature record[5]. **b**, Cariaco basin sediment reflectance, monitoring the latitudinal mean position of the ITCZ in the northwestern equatorial Atlantic[4]. **c**, $\Delta\delta^{18}O_{sw}$ of MD02-2529. **d**, Fe/Ca measurements, a proxy for riverine input, performed on sediments retrieved off Brazil[20]; black arrows indicate time intervals of the ITCZ southward expansion over Brazil based on well-dated speleothem growth intervals[19]. Grey vertical bars mark the North Atlantic H events. See Fig. 1 for the localization of tropical palaeoclimatic archives. YD, Younger Dryas; H1–H6, Heinrich events.

in the Caribbean and the EEP are considered (Supplementary Information). Our observations demonstrate that for all Heinrich events and the Younger Dryas the salinity increases are about two to three times larger on the Pacific side than on the Atlantic side of the isthmus (Supplementary Information). Our interpretation is that the salinity increases on both sides of the isthmus are modulated by the southward ITCZ shifts, whereas the signature of decreased inter-oceanic moisture flux is less salinity increase on the Atlantic side and more salinity increase on the Pacific side. This is precisely the anti-phased pattern of cross-isthmus moisture transport changes.

The MD02-2529 $\Delta\delta^{18}O_{sw}$ values imply that a northerly location of the ITCZ allowed enhanced moisture transport across the Panama isthmus, potentially leading to the build-up of salt in North Atlantic surface waters. By contrast, a southerly ITCZ position led to the orogenic blocking of moisture transport by the Andes[4]. This fresh water returned preferentially into the Atlantic Ocean, in particular through the Amazon basin drainage[20]. Inevitably, this must have lowered the salinity of low-latitude currents in the Atlantic Ocean, such as the North Brazil current, the Guyana current and the Caribbean current feeding the Gulf Stream.

The deuterium excess record from GRIP ice cores in Greenland shows that changes in their source temperature reflect southward shifts of the geographical location of moisture sources during stadials, presumably associated with southward displacements of the ITCZ[21]. This provides additional evidence for the key role played by the atmospheric water cycle and its related cross-isthmus moisture transport with respect to the H-DO variability. Some modelling studies attempted to reproduce the H-DO variability related to the formation of NADW by applying small freshwater anomalies of 0.03 Sv to the North Atlantic surface water[22] that are one order of magnitude smaller than the modern cross-isthmus vapour transport[1,13,14,18]. In the modern North Atlantic, low-salinity anomalies initially located at river mouths[23] are then advected in the Nordic Seas after a delay of several years with a probable influence on NADW formation[24]. If the ITCZ latitudinal cycles were indeed able to modulate the interoceanic salt contrast at the millennial timescale, then they could have contributed to the freshwater flux forcing applied in modelling experiments[22]. It is also possible that further north in the North Atlantic gyre other feedbacks could operate in a different manner[25]. The combined palaeoceanographic evidence and all identified feedback effects should be considered in modelling these events, that may enlighten our understanding of the modulation of NADW formation process and its related climatic effects.

We speculate that the moisture transport across Central America acts as a positive feedback on abrupt climatic changes. If true, the tropical climate variability is not limited to a passive response to the abrupt climatic changes observed in the North Atlantic region. Further tests of the implications of observed latitudinal and longitudinal hydrological shifts should be performed with models coupling atmosphere and ocean processes at the seasonal scale, and using highly resolved representations of Central and South-America in order to simulate realistic runoff fluxes.

METHODS

We estimated the regional SSS over the last 90 kyr BP by measuring $\delta^{18}O_{G.\ ruber}$ coupled with alkenone-based (using $U^{k'}_{37}$) and *G. ruber* Mg/Ca-based (using the cleaning method including the reductive step) sea surface palaeotemperatures data (Supplementary Information). To convert the $U^{k'}_{37}$ and the Mg/Ca into temperatures, we have used the calibration of refs 26 and 27, respectively. The lower Mg/Ca temperatures of the 20–25 kyr BP time interval might be caused by foraminiferal test dissolution (Fig. 2b, Supplementary Information). The $\delta^{18}O$ of sea water ($\delta^{18}O_{sw}$) was estimated by combining the $\delta^{18}O_{G.\ ruber}$ and $U^{k'}_{37}$-SST (Fig. 2c, Supplementary Information). To reconstruct past EEP salinities

($\Delta\delta^{18}O_{sw}$, Fig. 3c) we also removed the effect of global ice volume changes (ref. 17) from $\delta^{18}O_{sw}$. In the modern EEP, a $\delta^{18}O_{sw}$ drop of 1‰ corresponds to a salinity decrease of about 4 p.s.u. (ref. 18), remaining highly significant with respect to the typical error on salinity reconstructions[28] (Supplementary Information). The age model is constrained by a series of radiocarbon ages and by isotopic stratigraphy using the $\delta^{18}O$ temporal variations measured on two benthic foraminifer species (Fig. 2d, e; see Supplementary Information).

Received 18 October 2006; accepted 4 January 2007.

1. Zaucker, F. & Broecker, W. S. The influence of atmospheric moisture transport on the fresh water balance of the Atlantic drainage basin: General circulation model simulations and observations. *J. Geophys. Res.* **97,** 2765–2773 (1992).
2. Broecker, W. S., Bond, G., Klas, M., Bonani, G. & Wolfli, W. A salt oscillator in the glacial Atlantic? 1. The concept. *Paleoceanography* **5,** 469–477 (1990).
3. Bard, E. Climate shock: Abrupt changes over millennial time scales. *Phys. Today* **55,** 32–37 (2002).
4. Peterson, L. C., Haug, G. H., Hughen, K. A. & Röhl, U. Rapid changes in the hydrologic cycle of the tropical Atlantic during the Last Glacial. *Science* **290,** 1947–1951 (2000).
5. Stuiver, M. & Grootes, P. M. GISP2 oxygen isotope ratios. *Quat. Res.* **53,** 277–284 (2000).
6. Schmidt, M. W., Spero, H. J. & Lea, D. W. Links between salinity variation in the Caribbean and North Atlantic thermohaline circulation. *Nature* **428,** 160–163 (2004).
7. Bond, G. *et al.* Correlations between climate records from North Atlantic sediments and Greenland ice. *Nature* **365,** 143–147 (1993).
8. Wang, Y. J. *et al.* A high-resolution absolute-dated late Pleistocene monsoon record from Hulu Cave, China. *Science* **294,** 2345–2348 (2001).
9. Ivanochko, T. S. *et al.* Variations in tropical convection as an amplifier of global climate change at the millennial scale. *Earth Planet. Sci. Lett.* **235,** 302–314 (2005).
10. Broecker, W. S. Does the trigger for abrupt climate change reside in the ocean or in the atmosphere? *Science* **300,** 1519–1522 (2003).
11. Vidal, L. & Arz, H. in *Past Climate Variability Through Europe And Africa* (eds Battarbee, R. W. *et al.*) 31–44 (Springer, Dordrecht, 2004).
12. Liu, W. T. & Tang, W. Estimating moisture transport over oceans using space-based observations. *J. Geophys. Res.* **110,** D10101, doi:10.1029/2004JD005300 (2005).
13. Manabe, S. & Stouffer, R. J. Two stable equilibria of a coupled ocean-atmosphere model. *J. Clim.* **1,** 841–866 (1988).
14. Hostetler, S. W. & Mix, A. C. Reassessment of ice-age cooling of the tropical ocean and atmosphere. *Nature* **399,** 673–676 (1999).
15. Schmittner, A., Meissner, K. J., Eby, M. & Weaver, A. J. Forcing of the deep ocean circulation in simulations of the Last Glacial Maximum. *Paleoceanography* **17,** 1015, doi:10.1029/2001PA000633 (2002).
16. Benway, H. M., Mix, A. C., Haley, B. A. & Klinkhammer, G. P. Eastern Pacific Warm Pool paleosalinity and climate variability: 0–30 kyr. *Paleoceanography* **21,** PA3008, doi:10.1029/2005PA001208 (2006).
17. Waelbroeck, C. *et al.* Sea-level and deep water temperature changes derived from benthic foraminifera isotopic records. *Quat. Sci. Rev.* **21,** 295–305 (2002).
18. Benway, H. M. & Mix, A. C. Oxygen isotopes, upper-ocean salinity, and precipitation sources in the eastern tropical Pacific. *Earth Planet. Sci. Lett.* **224,** 493–507 (2004).
19. Wang, X. *et al.* Wet periods in northeastern Brazil over the past 210 kyr linked to distant climate anomalies. *Nature* **432,** 740–743 (2004).
20. Arz, H. W., Pätzold, J. & Wefer, G. Correlated millennial-scale changes in surface hydrography and terrigenous sediment yield inferred from last-glacial marine deposits off northeastern Brazil. *Quat. Res.* **50,** 157–166 (1998).
21. Masson-Delmotte, V. *et al.* GRIP deuterium excess reveals rapid and orbital-scale changes in Greenland moisture origin. *Science* **309,** 118–121 (2005).
22. Ganopolski, A. & Rahmstorf, S. Rapid changes of glacial climate simulated in a coupled climate model. *Nature* **409,** 153–158 (2001).
23. Masson, S. & Delecluse, P. Influence of the Amazon river runoff on the tropical Atlantic. *Phys. Chem. Earth B* **26,** 137–142 (2001).
24. Mignot, J. & Frankignoul, C. Interannual to interdecadal variability of sea surface salinity in the Atlantic and its link to the atmosphere in a coupled model. *J. Geophys. Res.* **109,** C04005, doi:10.1029/2003JC002005 (2004).
25. Schmidt, M. W., Vautravers, M. J. & Spero, H. J. Rapid subtropical North Atlantic salinity oscillations across Dansgaard-Oeschger cycles. *Nature* **443,** 561–564 (2006).
26. Sonzogni, C. *et al.* Temperature and salinity effects on alkenone ratios measured in surface sediments from the Indian Ocean. *Quat. Res.* **47,** 344–355 (1997).
27. Lea, D. W., Pak, D. K. & Spero, H. J. Climate impact of Late Quaternary equatorial Pacific sea surface temperature variations. *Science* **289,** 1719–1724 (2000).
28. Schmidt, G. A. Error analysis of paleosalinity calculations. *Paleoceanography* **14,** 422–429 (1999).

Supplementary Information is linked to the online version of the paper at www.nature.com/nature.

Acknowledgements We acknowledge support from INSU and the French Polar Institute IPEV, which provided the RV *Marion Dufresne* and the CALYPSO coring system used during the IMAGES VIII MONA cruise. Thanks to Y. Garcin and M. Siddall for discussion and reviews. Paleoclimate work at CEREGE is supported by grants from the CNRS, the ANR and the Gary Comer Science and Education Foundation.

Author Information Reprints and permissions information is available at www.nature.com/reprints. The authors declare no competing financial interests. Correspondence and requests for materials should be addressed to G.L. (leduc@cerege.fr) and E.B. (bard@cerege.fr).

SI1. EEP climatology

1) present-day atmospheric and oceanographic settings

Core MD02-2529 (08°12.33'N; 84°07.32'W; 1619 m water depth) was collected during the IMAGES VIII/MD 126 MONA oceanographic cruise (Fig. SF1a,b), off the Costa Rican margin. At the core location, SST are higher than 27°C and SSS are lower than 33.2 p.s.u. throughout the year (Fig. SF1c,d). The permanently low salinity of surface waters of the Panama Basin is maintained by the annual cycle of the ITCZ and its related surface currents. The dry and wet seasons occur between December and April (boreal winter), and between May and November (boreal summer), respectively (Fig. SF1e).

In March, northeasterly trade winds blow from the Atlantic area through low-level mountain gaps located onshore of the Tehuantepec Gulf (TG), the Nicaraguan Margin (NM) and the Panama Bight (PB), leading to a reduction in regional rainfall by shifting the ITCZ southward (Fig. SF1a,e, Fig. SF2). Wind-induced upwelling and mixing near the coast decrease the SST at TG, NM and PB (Fig. SF1a). No wind-induced upwelling affects the local hydrology at the coring site, which is situated in the lee of the Talamanca Cordillera (TC) culminating at between 3,000 and 4,000 m above sea level (Fig. SF1a). Northeasterly trades blowing across the NM and PB create westward flows of surface waters that advect into the North Equatorial Current (NEC) and the South Equatorial Current (SEC), respectively (Fig. SF1a). The westward advection of low-salinity (<32.5 p.s.u.) coastal currents - initially located close to the Colombian margin – causes a reduction in the SSS at the core location in March and April (Fig. SF1a,d) and make the surface circulation within the Panama Basin cyclonic. The absence of cloud cover leads to SST maxima during the dry season, remaining warmer than 28.5°C from December to May (Fig. SF1c).

The wet season between May and November is related to the northward shift of the ITCZ (e.g. September in Fig. SF1b and Fig. SF2), which leads to large amounts of rainfall during the summer monsoon over the MD02-2529 core location (Fig. SF1e, Fig. SF2). From May to July, the increasing cloud cover as well as the maximum development of the Costa Rica Dome [S1] lead to a SST drop, in turn responsible for a substantial weakening of deep atmospheric convection, at the origin of a mid-summer dry season occurring in July [S2] (see July in Fig. SF1e). Then, increased solar radiation over the warm pool occurring during the mid-summer dry season permits the reinvigoration of deep atmospheric convection, resulting in a second precipitation maximum between August and November. For these reasons, the

precipitation patterns of the wet season is bimodal [S2]. This wet season is in turn responsible for the general decrease in SSS between May and December (Fig. SF1d). Below the ITCZ, the trade winds weaken, allowing the eastward advection of the warm (29°C) and low-salinity waters (32 p.s.u.) of the North Equatorial Counter Current (NECC). This allows the mixing of NECC waters with EEP surface waters, while the NEC and SEC move northward and southward, respectively (Fig. SF1b). When it attains the Panama Bight, the NECC then flow southward, and the Panama Basin surface circulation becomes anticyclonic [S3]. During the wet season, the summer monsoon precipitation reduces the SSS from roughly 33 to 32 p.s.u. at MD02-2529 coring site (Fig. SF1d,e).

The regional SSS and the Central America rainfall patterns are unaffected by ENSO warm events [S4]. By contrast, El Niño years are marked rather by positive SST anomalies of 1 to 2°C in the Panama Basin. At the core location, these SST anomalies are imprinted in the $\delta^{18}O$ record of recent corals as a 0.2 to 0.4‰ negative anomaly, which is superimposed onto the mean annual variability of 0.9‰ of the $\delta^{18}O$ of corals due to the SSS seasonal cycle, and linked to the ITCZ dynamics [S4]. At the site of core MD02-2529, the millennial-scale $\delta^{18}O$ variability of 1‰ recorded by the surface-dwelling planktonic foraminifer *G. ruber* is hence unlikely to be affected by the ENSO dynamics.

Due to the high temperatures and low salinity of the surface waters, a strong pycnocline is set up between 30 and 70 m water depth at the core location (Fig. SF3). The seasonal variability of the pycnocline appears to be insignificant (Fig. SF3).

2) present-day seasonality of cross-isthmus freshwater fluxes

The seasonal timing as well as the exact amount of atmospheric freshwater flux that crosses Central America can be estimated from satellite data [S5]. The moisture transport is by definition the product of the precipitable water and an equivalent velocity integrated over the height of the atmosphere, i.e. the depth-averaged wind velocity weighted by humidity [S5]. For the Central America area, it is clear that predominant Easterlies situated in the Caribbean region are crossing the Central America during all seasons [S6], potentially leading to moisture export from the Atlantic throughout the year (Fig. SF2). However, the precipitable water content of the atmosphere on the Caribbean side of the Central America is reduced during the boreal winter (Fig. SF2). By contrast, during the boreal summer, the Caribbean easterlies transport water vapour from the tropical Atlantic toward the tropical Pacific Oceans. In addition, the ITCZ remains largely above the EEP during the wet season of boreal summer

(e.g. see Figure 1 of the manuscript). At the seasonal scale, the regional SSS variations in EEP are thus clearly triggered by the ITCZ-induced rainfall variations.

During the wet season, the rainfall received in the EEP is both derived from the atmospheric advection of "locally" (or from southerly winds) and "remotely" (or from northeasterly winds) derived moisture [S7]. The Figure SF2 illustrates the atmospheric content of precipitable water that allows tracking the source region of the atmospheric moisture that is precipitated at MD02-2529 coring site during summer. The precipitable water brought from the southerly trades is picked up after these winds have crossed the equator, i.e. above an oceanic region where SST considerably increases between the equatorial divergence and the warm pool. When they cross Central America, the northeasterly trades (i.e. carrying the water vapour across the Panama Isthmus) are already loaded by precipitable water evaporated over the Caribbean Sea. The EEP warm pool is a preferential site of precipitation for this fresh water transported from the Atlantic to the Pacific. A paleoclimatic approach based on SSS is thus suitable to reconstruct changes of rainfall, and hence of moisture transport across Central America.

3) atmospheric and oceanographic settings over the last 90 ky BP

In addition to atmospheric moisture transport across Central America, other processes such as horizontal mixing/advection, non-Atlantic moisture sources and mixing/upwelling from below the thermocline may have modulated the SSS fluctuations recorded in MD02-2529. However these processes are unlikely to be responsible for the main SSS variability patterns when it is kept in mind the SSS amplitudes – i.e. 2 to 4‰ – that we report at the millennial timescale:

- The NECC salinity in the central Pacific is only 1 p.s.u. lower than the surrounding northern and southern surface water masses up to at least 110°W of longitude. Farther east, the salinity then decreases simply because of the intense rainfall that occurs during the wet season, reaching salinities as low as 32.5 p.s.u. Even in the far eastern Pacific, the salinity gradient between the NECC and the broad regional surface waters of the entire EEP region remains largely lower than the SSS shifts that we report. Consequently, a very hypothetical collapse of the NECC could not be responsible for the SSS increase evidenced in core MD02-2529, in particular at times of Heinrich events. Advection processes are thus unlikely to explain the 2 to 4 p.s.u. recorded at the millennial timescale over the last 90 ky BP.

- About half of the rainfall over EEP was derived from the Caribbean Sea, as implied by the isotopic signature of the EEP precipitation [S7]. Because the ITCZ (and core MD02-2529) are located at the edge of the Central American coast, the atmospheric moisture transported by the northern trades must derive from the Caribbean Sea [S5] (see Fig. SF2). The other moisture sources (referred as "local" for the sake of simplicity) derive in fact from a region located in the northern hemisphere. Indeed, the equatorial cold tongue prevents the atmospheric loading because of the relatively cool SST at the equator (Fig. SF2, [S5]). Because of the geometry of the Panama Isthmus as well as the persistence of relatively cold equatorial temperature during glacial times [S8], it is unlikely that these local moisture sources dramatically changed in the past. Moreover, our SST record together with others from the tropical Pacific [S9] clearly show that temperature changes did not follow the H-DO variability at the millennial-centennial time scale. It is thus very unlikely that atmospheric moisture recharge followed by local precipitation would explain the EEP SSS signal recorded in core MD02-2529.

- At least two types of observations indicate that the observed surface waters variability was not driven by upwelling or mixing of the surface water column:

  Firstly, the Alkenone-derived SST temporal variations indicate that the sea surface remained warmer than 24°C over the last 90 ky BP (Fig. 2b), implying that subsurface waters were unlikely to have reached the 30m-thick mixed layer (see Fig. SF3 for the present-day thermocline depth).

  Secondly, for the last 90 ky BP, measurements of the $\delta^{13}C$ performed on the thermocline-dwelling species *Neogloboquadrina dutertrei* indicate that the $\delta^{13}C$ offset between *Globigerinoides ruber* and *N. dutertrei* varied independently of the large-amplitude fluctuations of $\delta^{18}O$ in *G. ruber*. Figure SF4 shows that the surface salinity proxy ($\Delta\delta^{18}O_{sw}$) is not correlated ($r^2 = 0.01$) with the upwelling proxy based on the $\delta^{13}C$ gradient between the two planktonic foraminifera (see [S10] for the planktonic foraminifera depth habitat and [S11] for the $\delta^{13}C_{DIC}$ gradients within the water column). It shows convincingly that the sea surface variability was not driven by subsurface waters, and that the pycnocline remained stable throughout the time interval studied.

SI2. Analytical procedures used to generate data available in Table 1

G. ruber was picked from the 250-355 μm size fraction. Samples of about 5 specimens were then reacted in H_3PO_4 at 70°C and the evolved CO_2 was analysed by a Finnigan Delta Advantage mass spectrometer at CEREGE. Stable isotopic ratios are reported in ‰ relative to the V-PDB standard, where $\delta^{18}O=[(^{18}O/^{16}O_{sample}/^{18}O/^{16}O_{standard})-1]*1000$. Analytical precision was better than ± 0.05‰ (± 1σ) based on repeated analyses of a NBS-19 limestone standard. We performed about 80 sample replicates out of a total of about 380 measurements, especially at key depths where rapid isotopic shifts are recorded. The temporal resolution of the *G. ruber* $\delta^{18}O$ dataset is ~250 years for the MIS 2 and 3 intervals.

Stable isotope measurements were also performed on the benthic foraminifera species *Cibicidoides wuellerstorfi* and *Uvigerina peregrina*, using the > 250 μm size fraction. The time resolution of *C. wuellerstorfi* is roughly the same as for the *G. ruber* dataset during MIS2 and 3, while the resolution of *U. peregrina* is three times lower. We performed about 50 sample replicates out of a total of about 330 measurements on *C. wuellerstorfi*, and 3 replicates from a total of about 120 measurements on *U. peregrina.*

Alkenones were extracted from bulk sediment, and analyses of C_{37} alkenones were performed by GC at CEREGE. The sample preparation and alkenone measurement techniques are described in Sonzogni *et al.* [S12]. The SST accuracy has been confirmed by an interlaboratory comparison study [S13]. Because temperatures are higher than 24°C throughout the sequence, we selected the calibration proposed by Sonzogni *et al.* [S12] (T (°C) = [$U^{k'}_{37}$-0.408]/0.019), which is based on low-latitude core-tops from the Indian Ocean including samples representing SST between 24 and 30°C. This $U^{k'}_{37}$ vs. SST linear equation has a lower slope (0.019/°C) than the slope of the linear regression (0.033/°C) based on core tops compiled from all oceans [S14]. Although the calibration of Sonzogni *et al.* has not been tested in the EEP, we believe it provides a better estimation for warm SST. Our choice of calibration is justified by a close inspection of the global compilation itself, as given by Müller *et al.* [S14], which suggests a flattening out of the relationship at high temperature. In addition, culture studies of different strains of *Gephyrocapsa oceanica* and *Emiliania huxleyi* [S15] and measurements in sinking particulates [S16, S17] strongly suggest that the true shape of the $U^{k'}_{37}$ vs. SST is probably sigmoïdal, with the $U^{k'}_{37}$ index converging asymptotically towards 0 and 1, for low and high temperatures, respectively. We estimate a temporal resolution of ~350 years for the $U^{k'}_{37}$ record in the MIS3 interval. The analytical

precision of replicated measurements is better than 0.01 $U^{k'}_{37}$ units, while the uncertainty of $U^{k'}_{37}$ SST is ± 0.7°C for the calibration used [S12]. Hence, the overall uncertainty is thus on the order of 1°C.

The Mg/Ca ratio was measured on *G. ruber*. About 30 shells were weighed prior to multi-step cleaning to estimate the possible influence of dissolution on Mg/Ca ratio. The shells were gently crushed and subjected to a cleaning procedure, which included a reductive step [S18, S19]. The reductive step appears to be crucial for the measurement of Mg/Ca in shells from Panama deep-sea sediments [S20]. Mg/Ca measurements were performed by ICP-OES (Jobin Yvon ULTIMA C) at CEREGE. The SST accuracy has been confirmed by an interlaboratory comparison study [S21]. Fe and Mn were also measured on these samples to monitor Mg contamination by remaining Fe-bearing clay minerals or Mn-bearing oxides and carbonates. With this method, the analytical precision on Mg/Ca is ca. 0.5 % (1σ). Foraminiferal Mg/Ca is converted to SST using the calibration of Lea *et al.* [S22] (Mg/Ca (mmol/mol) = 0.30exp[0.089*SST (°C)]). The uncertainty of SST reconstructed from Mg/Ca is estimated at ca. 1°C, similar than for $U^{k'}_{37}$.

Between 20 and 25 kyr BP, Mg/Ca temperatures are 2°C lower than $U^{k'}_{37}$ temperatures. One of the possible reasons for this offset is partial dissolution of shells, which lowers the foraminiferal Mg/Ca. The MIS2 is characterized by relatively high organic carbon content (i.e. about 3 % of dry sediment, Leduc et al., *in prep.*), that has probably induced metabolic-driven dissolution. The weights of *G. ruber* vary between 8 and 14 μg per individual through the studied time interval, and we did not observe any systematic trend with foraminiferal Mg/Ca (Table 1). However, since some shells contain pyrite, shell weight may not be an appropriate indicator of dissolution in this core.

We used $U^{k'}_{37}$ paleothermometry for the high-resolution calculation of the $\delta^{18}O$ of seawater. To obtain a SST value for each $\delta^{18}O_{G.ruber}$ measurement, the $U^{k'}_{37}$ SST record has been linearly interpolated (the depth resolution is 2 to 5 cm, and 5 cm, respectively, for these markers, see Table 1). In our case, such an interpolation is justified because SST does not vary at high frequency, unlike $\delta^{18}O_{G.ruber}$. Although alkenones are carried by finer sized particles than foraminiferal tests, the sedimentation rate – which is higher than 10 cm.ky^{-1}- considerably decreases the phase shift between the two different size fractions and reduces the signal attenuation due to mixing of deep-sea sediment by benthic organisms [S23]. Besides, sediment trap studies of the Panama Basin have pointed out that the maximum flux of *G.*

ruber is concurrent with the main phytoplanktonic bloom during the summer months [S24]. This suggests that, at least for this survey, the $\delta^{18}O_{G.ruber}$ and alkenones should have recorded comparable hydrological patterns with respect to the annual variability of SST and SSS. Moreover, long-term variations of both Mg/Ca and $U_{37}^{k'}$ paleothermometers show roughly the same amplitude and phasing, thus justifying the use of alkenones to derive fluctuations in seawater $\delta^{18}O$.

To estimate the $\delta^{18}O$ of seawater ($\delta^{18}O_{sw}$), we used the paleotemperature equation calibrated for symbiont-bearing planktonic foraminifera [S25] in order to correct the $\delta^{18}O_{G.ruber}$ values for temperature influence (Fig. 2c). However, obtaining a proxy for regional SSS variations that reflect the rainfall variations strictly speaking (i.e. the $\Delta\delta^{18}O_{sw}$, see Figure 3c) also requires further correction from the global $\delta^{18}O_{sw}$ due to variations of continental ice volumes, that is linearly related to sea level variations. To reconstruct the $\Delta\delta^{18}O_{sw}$, we removed the long-term ice volume signal [S26]. Even if sea level fluctuations could have occurred at the millennial scale [S27, S28] (and then could have induced global oceanic $\delta^{18}O_{sw}$ variations of amplitude higher than that of Waelbroeck et al., [S26]) our calculated $\Delta\delta^{18}O_{sw}$ cannot be explained in terms of high-frequency sea-level fluctuations, which are one order of magnitude smaller than our $\Delta\delta^{18}O_{sw}$ record. Also, in the equatorial Pacific Ocean, regional transient changes in the $\delta^{18}O_{sw}$ due to deglacial spikes are not expected because of the long-term mixing time of $\delta^{18}O_{sw}$ within the ocean [S29]. Then, our $\Delta\delta^{18}O_{sw}$ record properly represents past regional SSS variations that are linked to the ITCZ dynamics.

Based on the modern $\delta^{18}O_{sw}$/salinity linear relationship for Panama basin surface waters [S7], a $\Delta\delta^{18}O_{sw}$ decrease of 0.5 to 1‰ would correspond to a salinity decrease of about 2 to 4 p.s.u. It is also important to note that in the case of variable water transport, no $\delta^{18}O_{sw}$/salinity relationship changes are expected [S7]. Paleosalinities reconstructed from $U_{37}^{k'}$ paleothermometry lead typically to errors of 1.4 p.s.u. under tropical climates [S30]. In the case of MD02-2529, the systematic fluctuations of 2 to 4 p.s.u. at the millennial timescale remain highly significant.

SI3. Age control

The age model for core MD02-2529 is based on calibrated radiocarbon ages for the last 40 kyr BP and on benthic foraminifera stratigraphy for the rest of the sequence (cf. Fig. 2d and Table 2).

Eleven radiocarbon measurements were performed on the planktonic foraminifer species *N. dutertrei* (Table 2). Where possible, several intervals were also dated using *G. ruber* (Table 2), to test for any age differences between the two species. *N. dutertrei* has a slightly deeper-water habitat than *G. ruber* and may record some additional age reservoir effect, linked to different water masses [S10]. At the present day, the upper 200 m of the EEP are relatively homogeneous in terms of $\Delta^{14}C$ [S31], despite the sharp pycnocline at around 50 m depth (Fig. SF3), indicating that *N. dutertrei* is bathed in the newly formed equatorial undercurrent subsurface waters. The differences between the ^{14}C ages of the two species do not systematically display a $\Delta^{14}C$ offset due to surface water stratification, and are of the same order as the age measurement uncertainty (Table 2). Consequently, to simplify the construction of the age model, we only used ^{14}C dates obtained from *N. dutertrei*, and two ^{14}C ages at the 356-357 cm and 357-358 cm core-depth intervals have been averaged (Table 2).

For the construction of the age model, we used the MARINE04 calibration curve to convert the ^{14}C ages into calendar ages for the last 25,000 ^{14}C years BP [S32] and the CALIB 5.3 radiocarbon calibration program [S33]. We have used a ΔR of 50±49 for the surface water mass at the core location (ΔR for the MD02-2529 core location is available at http://calib.qub.ac.uk/marine/). For older radiocarbon ages, we applied the polynomial equation proposed by Bard *et al.* [S34], which has been calculated by stratigraphic tuning on GISP2 chronology [S35].

To obtain better constraints beyond the ^{14}C age limit, we also made use of the benthic $\delta^{18}O$ record (Fig. 2d). A widely observed feature of high-resolution benthic oxygen isotopic records is the succession of several "triangular shapes" during MIS3, which mimics the Antarctica paleotemperature variations (e.g. [S28, S36]), and which likely represent fluctuations of ice volume and sea level [S27, S28], and/or deep sea temperature variations [S37]. In the MD02-2529 core, the benthic oxygen isotopes - measured on *C. wuellerstorfi* and on *U. peregrina* - also yield typical triangle-shaped records (Fig. 2e). Following the approach of Shackleton *et al.* [S28], we took additional age control points from the correlation between the benthic $\delta^{18}O$ minima and the Antarctic warm events. These warm events are

dated at around 46, 53 and 58 kyr BP for A2, A3 and A4, respectively, which are themselves tuned to the GISP2 chronology [S38]. We are quite confident about our MIS3 chronology because (1) MD02-2529 $\delta^{18}O$ benthic records made on two different species both mimic the $\delta^{18}O$ profile of Byrd ice core; (2) it yields relatively stable sedimentation rates throughout the sequence; (3) it provides a smooth connection between the oldest radiocarbon age and the age of Antarctic event A1 (i.e. 39 kyr BP); (4) it provides a good match between the Cariaco reflectance record [S39] and the $\delta^{18}O$ record of core MD02-2529. Even if this match is already satisfactory, it could even be improved by fine tuning by a few centuries the chronology of core MD02-2529, especially for the early MIS3. However we decided not to apply further matching in order to keep each tropical record on its own independent chronology. The 60-90 kyr BP interval is dated by correlating the benthic $\delta^{18}O$ record to a reference stack of benthic foraminifera $\delta^{18}O$ records [S40]. The mean sedimentation rate is ~13 $cm.kyr^{-1}$ for MIS2 and 3.

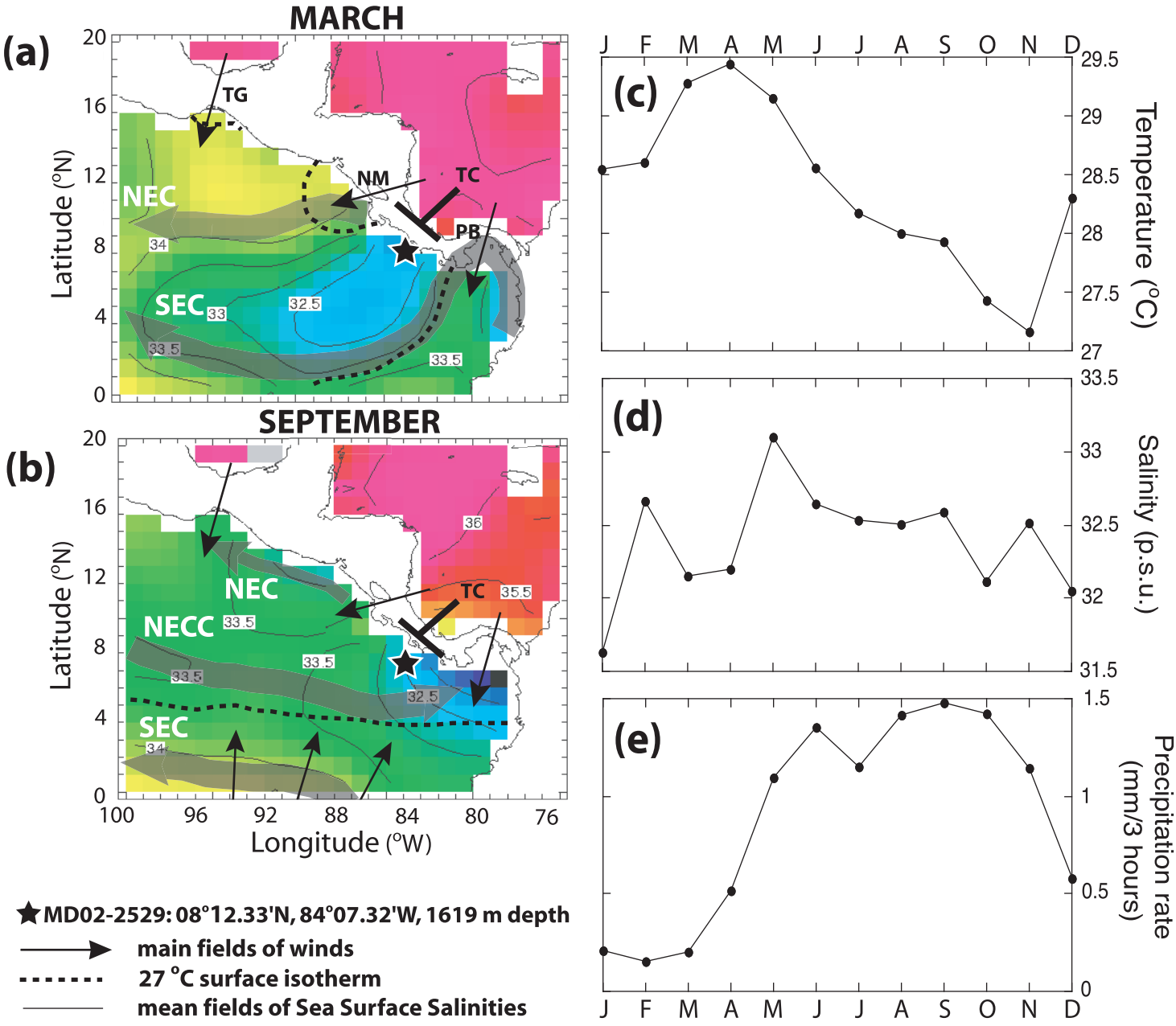

Figure SF1:
Temporal variations of modern atmospheric and oceanic settings (a, b) in the Eastern Equatorial Pacific Ocean (adapted from [S1]) and (c, d, e) at core location (data extracted from [S41] for SST and SSS, and [S42] for precipitation rates. Data are available online at http://ingrid.ldeo.columbia.edu). Simplified map representing seasonal variations of SSS (colors and their corresponding values in p.s.u., [S41]) for March (a) and September (b). The black star corresponds to the MD02-2529 core location. Black arrows represent the main seasonal wind fields. The thick dashed lines indicate the position of the 27°C surface isotherm [S41]. Monthly mean atmospheric and oceanic extracted data are taken for latitudes and longitudes between 7.5°N to 8.5 °N and 83.5°W to 84.5°W. (c): SST; (d): SSS; (e): precipitation rate. NEC for North Equatorial Current, NECC for North Equatorial Countercurrent, SEC for South Equatorial Current, TC for Talamanca Cordillera, TG for Tehuantepec Gulf, NM for Nicaraguan Margin and PB for Panama Basin.

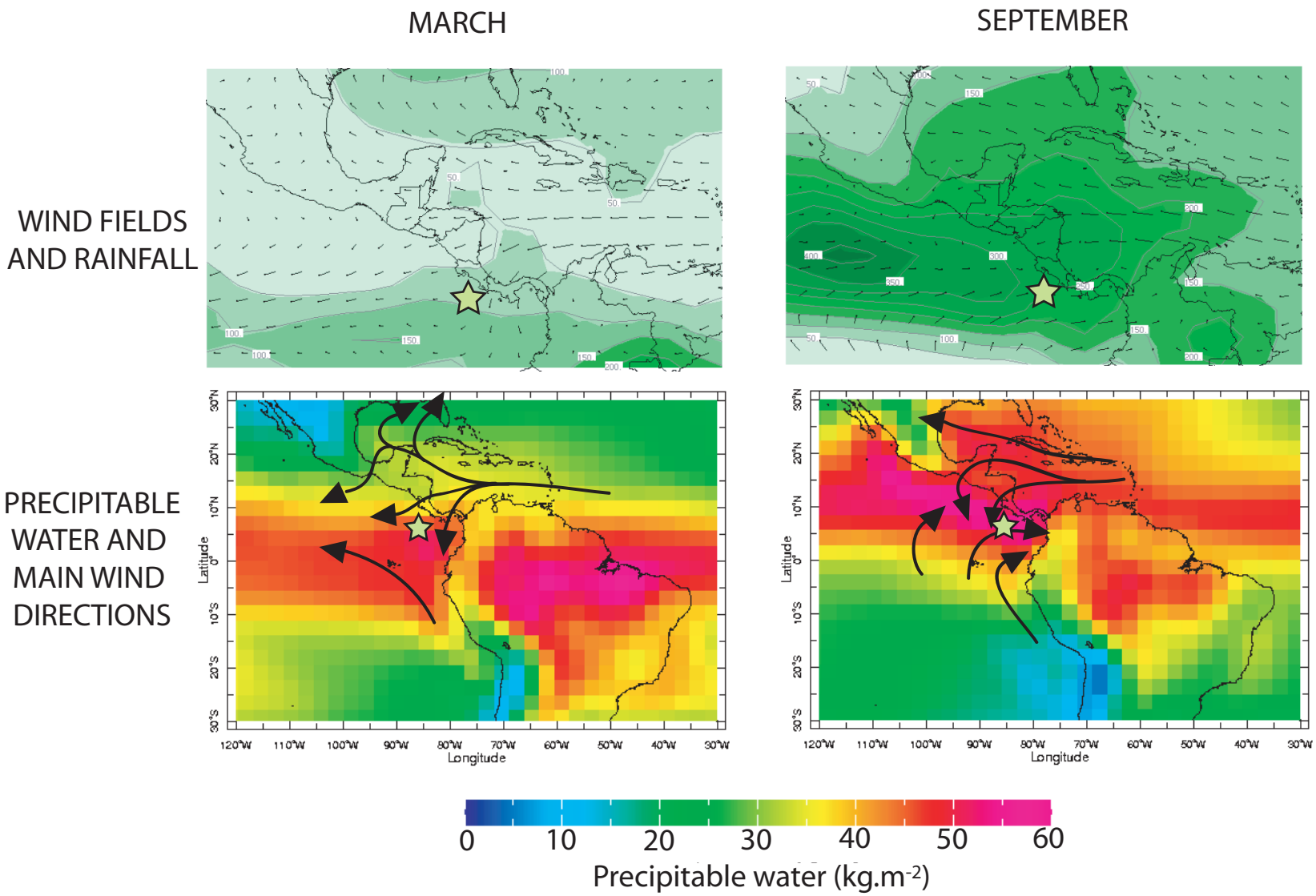

Figure SF2:
Upper panels: seasonal extremes of wind vectors and precipitation fields (green colors and their related precipitation rates in mm/month) for March (left panels) and September (right panels). Bottom panels: precipitable water (i.e. atmospheric humidity) for March (left panels) and September (right panels). The black arrows in the bottom panels indicate the main wind directions. Data were retrieved from the NCEP/NCAR reanalysis dataset and are available online at http://ingrid.ldeo.columbia.edu. Note that in the Caribbean, the easterlies strength remains roughly constant, but winds are carrying dry and wet air during boreal winter and summer, respectively.

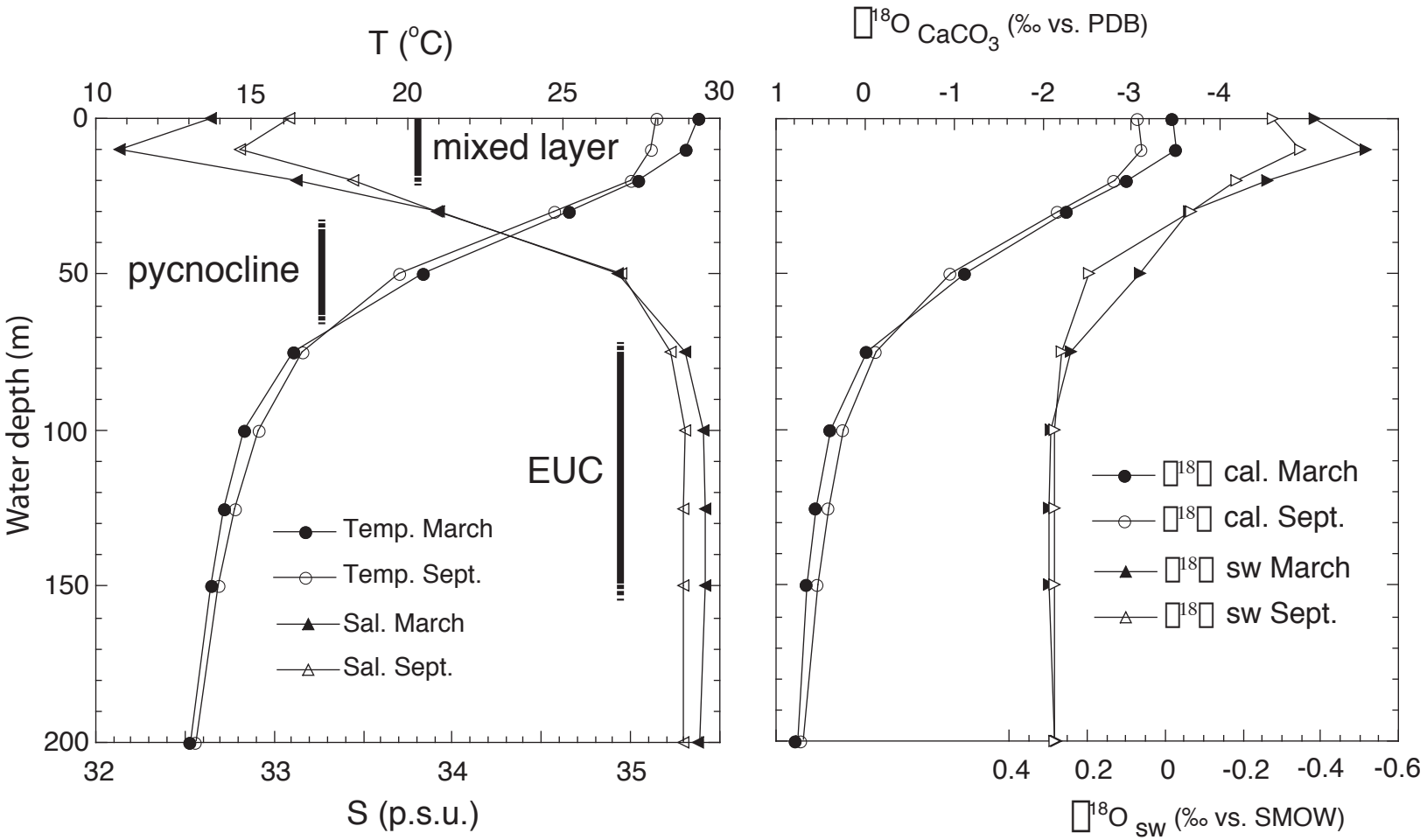

Figure SF3:
Mean monthly hydrological records for March (black symbols) and September (open symbols) of the upper 200 m depth at core location. Temperatures (circles) and Salinity (triangles) were extracted from the WOA01 database [S41] at the same location as described for Figure SF1. The black vertical bars localize the two main water masses (EEP surface waters and Equatorial Undercurrent referred as EUC), and the sharp pycnocline between 30 and 70 m depth. The values of $\delta^{18}O$ (right panel) calculated for the seawater (triangles) and for the $CaCO_3$ at equilibrium (circles) are based on the same dataset [S41]. To convert the salinity to $\delta^{18}O_{sw}$ we used the $\delta^{18}O_{sw}$-Salinity relationship ($\delta^{18}O_{sw}$ (‰) = 0.253 S (p.s.u.) - 8.52 for the upper 40m water depth; $\delta^{18}O_{sw}$ (‰) = 0.471 S (p.s.u.) – 16.15 for the 40-200 m water depth interval [S7]). The $\delta^{18}OCaCO_3$ was calculated with the paleotemperature equation [S43] (T (°C) = 16.9 – 4.38 ($\delta^{18}OCaCO_3$ - $\delta^{18}O_{sw}$) + 0.1 ($\delta^{18}OCaCO_3$ - $\delta^{18}O_{sw}$)^2). The calculated $\delta^{18}OCaCO_3$ for surface waters are –3.4 and –3.1 ‰ for March and September respectively. It is in agreement with the $\delta^{18}OCaCO_3$ measured on the surface-dwelling planktonic species *G. ruber* retrieved in sediment traps in Panama Basin, that approximately vary between –3.4 an –2.8 ‰ through the year [S44].

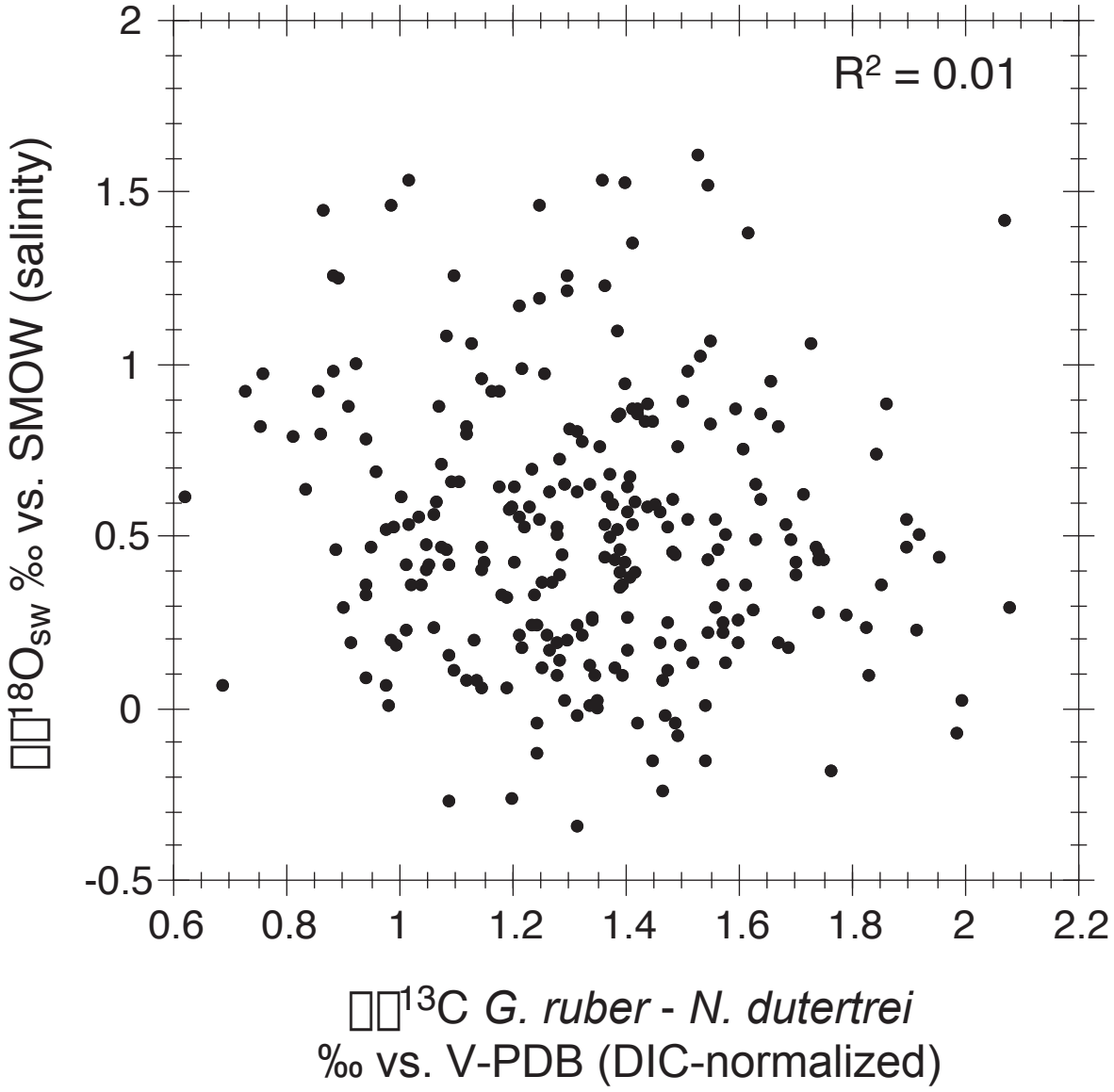

Figure SF4:
□□$^{18}O_{sw}$ (i.e. SSS) as a function of the □^{13}C gradient between *G. ruber* and *N. dutertrei* (□□^{13}C, i.e. a proxy for upwelling/mixing). The □^{13}C measured on planktonic foraminifera have been normalized to the □^{13}C of Dissolved Inorganic Carbon (DIC) by assuming a constant offset of +0.94 ‰ for *G. ruber* and –0.5 ‰ for *N. dutertrei* [S10, S45]. Note that no relationship exists between both proxies, indicating that the SSS is unlikely to have been influenced by upwelling and/or mixing.

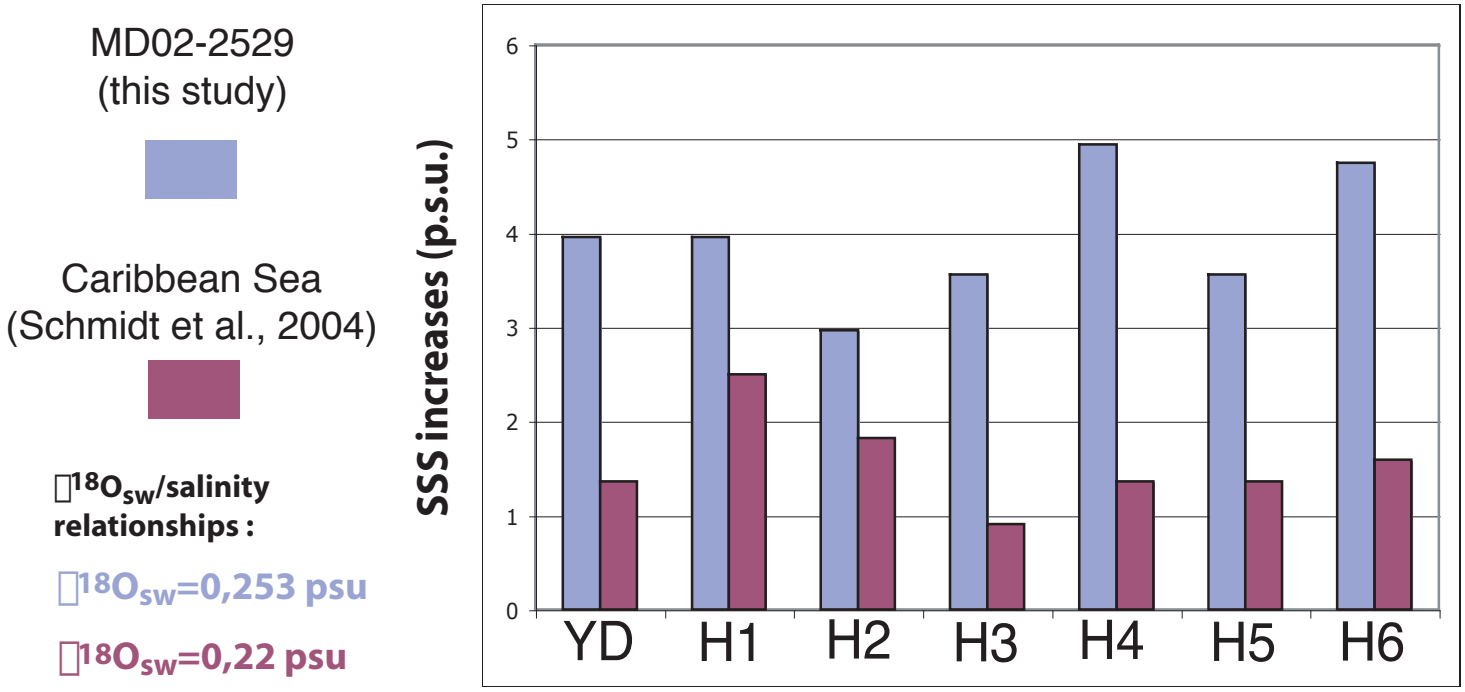

Figure SF5:
Comparison between salinity increases in MD02-2529 (this study) and in the Caribbean Sea [S46], reconstructed for the six Heinrich events and the Younger Dryas. These seven events are all characterized by a southward shift of the ITCZ, inducing a salinity increase in both records. A second-order antiphasis signature of the reduced moisture transport induces the amplitude differences recorded across the Panama Basin at these times. The water vapour that is not efficiently transferred from the Atlantic toward the Pacific Ocean leads to a freshening of the Caribbean Sea, and to an increased salinity at MD02-2529 core location.

Table 1:

Results from MD02-2529 core.

MD02-2529 depth (cm)	age (yr BP)	d18O G. ruber (VPDB‰)	Uk'37	Uk' 37-SST (°C)	Mg/Ca (mmol.mol-1)	Mg/Ca-SST (°C)	ruber weight (μg.ind-1)
3	112	-3.00	0.954	28.7	n.d.	n.d.	n.d.
10	372	-3.00	0.952	28.6	n.d.	n.d.	n.d.
20	629	-2.70	0.961	29.1	n.d.	n.d.	n.d.
30	858	-3.16	0.962	29.2	n.d.	n.d.	n.d.
40	1088	-3.48	0.96	29.1	n.d.	n.d.	n.d.
50	1317	-3.39	0.95	28.5	n.d.	n.d.	n.d.
60	1546	-2.58	0.969	29.5	n.d.	n.d.	n.d.
70	1775	-2.74	0.964	29.3	n.d.	n.d.	n.d.
80	2004	-2.98	0.954	28.7	n.d.	n.d.	n.d.
90	2233	-2.91	0.941	28.1	n.d.	n.d.	n.d.
100	2462	-3.10	0.942	28.1	n.d.	n.d.	n.d.
110	2691	-3.14	0.939	27.9	n.d.	n.d.	n.d.
120	2920	-2.89	0.94	28.0	n.d.	n.d.	n.d.
130	3150	-2.74	0.937	27.8	n.d.	n.d.	n.d.
136	3287	n.d.	n.d.	n.d.	3.80	27.6	n.d.
140	3425	-3.18	0.941	28.1	n.d.	n.d.	n.d.
148	3701	-3.01	0.939	27.9	n.d.	n.d.	n.d.
160	4116	-2.64	0.957	28.9	n.d.	n.d.	n.d.
170	4461	-3.04	0.94	28.0	n.d.	n.d.	n.d.
176	4668	-2.88	0.936	27.8	n.d.	n.d.	n.d.
190	5152	-2.60	0.932	27.6	n.d.	n.d.	n.d.
200	5497	-2.33	0.923	27.1	n.d.	n.d.	n.d.
210	5842	-2.39	0.938	27.9	n.d.	n.d.	n.d.
220	6188	-2.82	0.925	27.2	n.d.	n.d.	n.d.
230	6533	-2.47	0.929	27.4	n.d.	n.d.	n.d.
235	6705	n.d.	0.924	27.2	n.d.	n.d.	n.d.
240	6878	-2.51	n.d.	n.d.	n.d.	n.d.	n.d.
250	7223	-2.71	0.928	27.4	n.d.	n.d.	n.d.
260	7569	-2.68	0.941	28.1	n.d.	n.d.	n.d.
270	7914	-2.68	0.939	27.9	n.d.	n.d.	n.d.
280	8259	n.d.	0.94	28.0	n.d.	n.d.	n.d.
290	8605	-2.63	0.936	27.8	n.d.	n.d.	n.d.
299	8915	n.d.	0.935	27.7	n.d.	n.d.	n.d.
303	9054	-2.26	0.934	27.7	n.d.	n.d.	n.d.
314	9433	-2.17	0.938	27.9	n.d.	n.d.	n.d.
323	9744	n.d.	0.925	27.2	n.d.	n.d.	n.d.
333	10089	n.d.	0.92	26.9	n.d.	n.d.	n.d.
343	10435	-2.37	0.936	27.8	n.d.	n.d.	n.d.
353	10780	-2.23	0.924	27.2	n.d.	n.d.	n.d.
359	10987	n.d.	0.942	28.1	n.d.	n.d.	n.d.
363	11175	-2.38	0.923	27.1	n.d.	n.d.	n.d.
369	11468	-2.23	0.93	27.5	n.d.	n.d.	n.d.
373	11663	-1.47	0.93	27.5	n.d.	n.d.	n.d.
379	11955	-1.65	0.931	27.5	n.d.	n.d.	n.d.
383	12150	-1.18	0.933	27.6	n.d.	n.d.	n.d.
389	12443	-1.31	0.919	26.9	n.d.	n.d.	n.d.
393	12638	-2.13	0.922	27.1	n.d.	n.d.	n.d.
399	12930	-1.82	0.936	27.8	n.d.	n.d.	n.d.

403	13125	-1.68	0.922	27.1	n.d.	n.d.	n.d.
409	13420	-1.60	0.916	26.7	n.d.	n.d.	n.d.
411	13522	-1.52	0.911	26.5	n.d.	n.d.	n.d.
414	13674	-1.60	n.d.	n.d.	n.d.	n.d.	n.d.
419	13927	-1.55	0.91	26.4	n.d.	n.d.	n.d.
423	14129	-1.69	0.908	26.3	n.d.	n.d.	n.d.
429	14433	-1.97	n.d.	n.d.	n.d.	n.d.	n.d.
429	14433	n.d.	0.905	26.2	n.d.	n.d.	n.d.
433	14635	-1.87	0.907	26.3	n.d.	n.d.	n.d.
439	14939	-1.72	0.912	26.5	n.d.	n.d.	n.d.
443	15141	-1.54	0.912	26.5	n.d.	n.d.	n.d.
449	15445	-1.16	0.91	26.4	n.d.	n.d.	n.d.
453	15648	-1.04	0.913	26.6	n.d.	n.d.	n.d.
455	15749	-1.22	n.d.	n.d.	n.d.	n.d.	n.d.
459	15951	-1.25	0.903	26.1	n.d.	n.d.	n.d.
463	16154	-0.82	0.902	26.0	n.d.	n.d.	n.d.
465	16255	-0.78	n.d.	n.d.	n.d.	n.d.	n.d.
469	16457	-0.96	0.9	25.9	n.d.	n.d.	n.d.
473	16681	-1.34	0.902	26.0	3.65	27.2	13.03
475	16796	-0.84	n.d.	n.d.	n.d.	n.d.	n.d.
479	17027	-0.99	0.905	26.2	n.d.	n.d.	n.d.
483	17258	-1.28	0.903	26.1	n.d.	n.d.	14.45
485	17373	-0.81	n.d.	n.d.	n.d.	n.d.	n.d.
489	17604	-0.74	0.903	26.1	n.d.	n.d.	n.d.
493	17835	-1.06	0.903	26.1	n.d.	n.d.	13.61
495	17950	-1.00	n.d.	n.d.	n.d.	n.d.	14.23
499	18181	-0.96	0.901	25.9	3.05	25.2	13.62
503	18412	-1.28	0.894	25.6	3.02	25.1	13.66
505	18527	-0.90	n.d.	n.d.	n.d.	n.d.	n.d.
509	18758	-1.49	0.884	25.1	n.d.	n.d.	14.49
513	18989	-1.43	0.888	25.3	n.d.	n.d.	13.97
515	19104	-1.13	n.d.	n.d.	n.d.	n.d.	n.d.
519	19342	-1.35	0.895	25.6	n.d.	n.d.	n.d.
523	19601	-1.24	0.891	25.4	n.d.	n.d.	13.00
525	19731	-0.38	n.d.	n.d.	n.d.	n.d.	11.37
529	19990	-0.79	0.908	26.3	n.d.	n.d.	13.15
533	20249	-1.23	0.906	26.2	n.d.	n.d.	n.d.
534	20314	n.d.	n.d.	n.d.	3.62	27.1	n.d.
535	20379	-1.24	n.d.	n.d.	n.d.	n.d.	n.d.
539	20638	-1.17	0.911	26.5	2.82	24.4	12.52
543	20897	-1.41	0.896	25.7	n.d.	n.d.	n.d.
545	21027	-0.90	n.d.	n.d.	n.d.	n.d.	n.d.
549	21286	-1.53	0.909	26.4	2.88	24.6	13.25
553	21545	-1.14	0.905	26.2	n.d.	n.d.	n.d.
555	21675	-1.43	n.d.	n.d.	n.d.	n.d.	n.d.
559	21934	-1.50	0.912	26.5	n.d.	n.d.	n.d.
561	22063	-0.60	0.903	26.1	n.d.	n.d.	n.d.
564	22258	-0.41	0.905	26.2	2.80	24.3	16.22
565	22322	-0.56	0.906	26.2	n.d.	n.d.	n.d.
569	22582	-0.83	n.d.	n.d.	n.d.	n.d.	n.d.
573	22841	-1.02	0.901	25.9	n.d.	n.d.	12.94
575	22970	-0.96	n.d.	n.d.	n.d.	n.d.	12.60
579	23229	-1.45	0.9	25.9	n.d.	n.d.	n.d.
583	23489	-1.58	0.902	26.0	2.56	23.3	14.52
585	23618	-1.13	n.d.	n.d.	n.d.	n.d.	n.d.
589	23877	-1.22	0.905	26.2	n.d.	n.d.	14.45
593	24152	-1.18	0.895	25.6	n.d.	n.d.	13.17
595	24294	-0.96	n.d.	n.d.	n.d.	n.d.	12.33

599	24577	-0.86	0.894	25.6	n.d.	n.d.	12.20
603	24861	-0.87	0.891	25.4	3.12	25.4	11.46
605	25003	-1.15	n.d.	n.d.	n.d.	n.d.	n.d.
609	25286	-1.23	0.886	25.2	3.14	25.5	11.35
613	25570	-1.11	0.882	24.9	3.04	25.2	11.31
614	25641	n.d.	n.d.	n.d.	3.25	25.9	n.d.
615	25711	-1.37	n.d.	n.d.	n.d.	n.d.	n.d.
619	25995	-1.18	0.875	24.6	3.11	25.4	9.45
623	26279	-1.42	0.895	25.6	3.20	25.7	11.50
625	26420	-1.04	n.d.	n.d.	n.d.	n.d.	n.d.
629	26704	-1.18	0.892	25.5	3.07	25.3	10.79
633	26988	-1.20	0.896	25.7	n.d.	n.d.	n.d.
635	27129	-0.94	n.d.	n.d.	n.d.	n.d.	n.d.
639	27413	-1.25	0.879	24.8	n.d.	n.d.	n.d.
643	27697	-1.12	0.886	25.2	n.d.	n.d.	n.d.
645	27838	-0.89	n.d.	n.d.	n.d.	n.d.	n.d.
649	28122	-1.38	0.89	25.4	n.d.	n.d.	n.d.
653	28406	-1.12	0.891	25.4	n.d.	n.d.	n.d.
655	28547	-1.57	n.d.	n.d.	n.d.	n.d.	n.d.
659	28831	-1.62	0.891	25.4	n.d.	n.d.	n.d.
663	29115	-1.26	0.901	25.9	n.d.	n.d.	n.d.
665	29256	-1.03	n.d.	n.d.	n.d.	n.d.	14.13
669	29540	-0.71	0.904	26.1	n.d.	n.d.	n.d.
673	29823	-1.55	0.906	26.2	n.d.	n.d.	n.d.
675	29965	-0.84	n.d.	n.d.	n.d.	n.d.	n.d.
679	30249	-1.11	0.886	25.2	n.d.	n.d.	n.d.
683	30546	-1.25	0.883	25.0	n.d.	n.d.	n.d.
685	30697	-0.44	n.d.	n.d.	n.d.	n.d.	n.d.
688	30923	n.d.	n.d.	n.d.	2.97	24.9	n.d.
689	30999	-1.11	0.886	25.2	n.d.	n.d.	n.d.
693	31300	-1.21	0.887	25.2	n.d.	n.d.	n.d.
695	31450	-1.30	n.d.	n.d.	n.d.	n.d.	n.d.
699	31751	-1.18	0.884	25.1	3.01	25.1	14.86
703	32053	-1.58	n.d.	n.d.	n.d.	n.d.	14.50
705	32203	-1.34	n.d.	n.d.	n.d.	n.d.	13.37
709	32504	-1.99	0.878	24.7	n.d.	n.d.	16.27
711	32655	-1.48	0.887	25.2	n.d.	n.d.	12.76
715	32956	-1.34	0.89	25.4	n.d.	n.d.	n.d.
719	33257	-0.89	0.888	25.3	3.33	26.2	14.26
723	33558	-1.41	0.893	25.5	n.d.	n.d.	15.62
725	33708	-1.60	n.d.	n.d.	n.d.	n.d.	n.d.
729	34009	-1.14	0.888	25.3	n.d.	n.d.	n.d.
733	34310	-1.38	0.905	26.2	n.d.	n.d.	12.23
735	34461	-1.01	n.d.	n.d.	n.d.	n.d.	n.d.
739	34762	-1.51	0.904	26.1	n.d.	n.d.	n.d.
743	35063	-1.92	n.d.	n.d.	3.53	26.8	14.90
745	35213	-1.75	n.d.	n.d.	n.d.	n.d.	n.d.
749	35515	-1.70	0.906	26.2	n.d.	n.d.	n.d.
753	35816	-1.94	0.905	26.2	n.d.	n.d.	14.67
755	35966	-1.16	n.d.	n.d.	n.d.	n.d.	n.d.
759	36267	-1.51	0.903	26.1	n.d.	n.d.	n.d.
763	36568	-1.41	0.899	25.8	n.d.	n.d.	15.10
765	36719	-0.92	n.d.	n.d.	n.d.	n.d.	12.47
769	37020	-1.27	0.902	26.0	n.d.	n.d.	n.d.
773	37321	-1.00	0.91	26.4	n.d.	n.d.	15.87
775	37471	-1.10	n.d.	n.d.	n.d.	n.d.	n.d.
779	37772	-1.25	0.913	26.6	n.d.	n.d.	n.d.
783	38073	-1.56	0.919	26.9	3.87	27.8	12.16

785	38224	-1.38	n.d.	n.d.	n.d.	n.d.	n.d.
789	38525	-1.94	0.917	26.8	n.d.	n.d.	12.17
793	38799	-1.62	0.924	27.2	n.d.	n.d.	13.00
795	38927	-1.86	n.d.	n.d.	n.d.	n.d.	n.d.
799	39184	-0.75	0.924	27.2	3.77	27.5	13.72
803	39442	-1.00	0.918	26.8	n.d.	n.d.	n.d.
805	39570	-1.13	n.d.	n.d.	n.d.	n.d.	n.d.
809	39827	-0.99	0.914	26.6	n.d.	n.d.	n.d.
813	40085	-1.16	0.906	26.2	n.d.	n.d.	13.12
815	40213	-1.31	n.d.	n.d.	n.d.	n.d.	n.d.
819	40470	-1.65	0.903	26.1	n.d.	n.d.	13.27
823	40728	-1.40	0.9	25.9	n.d.	n.d.	n.d.
825	40856	-1.29	n.d.	n.d.	n.d.	n.d.	n.d.
829	41113	-1.34	0.89	25.4	n.d.	n.d.	n.d.
830	41178	-1.35	0.898	25.8	3.04	25.2	13.60
834	41435	-1.16	0.908	26.3	n.d.	n.d.	n.d.
835	41499	-1.41	n.d.	n.d.	n.d.	n.d.	n.d.
839	41756	-1.70	0.896	25.7	n.d.	n.d.	15.41
843	42014	-1.49	0.9	25.9	n.d.	n.d.	n.d.
845	42142	-1.33	n.d.	n.d.	n.d.	n.d.	n.d.
849	42399	-1.47	0.897	25.7	n.d.	n.d.	n.d.
853	42656	-1.25	0.902	26.0	n.d.	n.d.	n.d.
855	42785	-1.56	n.d.	n.d.	n.d.	n.d.	n.d.
859	43042	-1.42	0.892	25.5	n.d.	n.d.	n.d.
863	43299	-1.23	0.891	25.4	n.d.	n.d.	12.94
865	43428	-1.26	n.d.	n.d.	n.d.	n.d.	n.d.
869	43685	-1.62	0.874	24.5	n.d.	n.d.	n.d.
873	43942	-1.21	0.875	24.6	n.d.	n.d.	n.d.
875	44071	-1.17	n.d.	n.d.	n.d.	n.d.	n.d.
879	44328	-1.67	0.873	24.5	n.d.	n.d.	n.d.
883	44585	-1.43	0.873	24.5	2.79	24.2	14.75
885	44714	-1.56	n.d.	n.d.	n.d.	n.d.	n.d.
889	44971	-1.39	0.871	24.4	n.d.	n.d.	n.d.
893	45228	-1.66	0.873	24.5	n.d.	n.d.	n.d.
895	45357	-1.46	n.d.	n.d.	n.d.	n.d.	n.d.
899	45614	-1.84	0.868	24.2	n.d.	n.d.	n.d.
903	45871	-1.79	0.887	25.2	3.19	25.7	13.09
905	46000	-1.52	n.d.	n.d.	n.d.	n.d.	n.d.
909	46311	-1.22	0.882	24.9	n.d.	n.d.	n.d.
913	46622	-1.06	0.885	25.1	n.d.	n.d.	n.d.
915	46778	-0.93	n.d.	n.d.	n.d.	n.d.	n.d.
919	47089	-1.63	0.894	25.6	n.d.	n.d.	n.d.
923	47400	-1.16	0.895	25.6	n.d.	n.d.	n.d.
925	47556	-1.51	n.d.	n.d.	n.d.	n.d.	n.d.
929	47867	n.d.	0.899	25.8	n.d.	n.d.	n.d.
933	48178	-1.36	0.898	25.8	n.d.	n.d.	n.d.
935	48333	-1.52	n.d.	n.d.	n.d.	n.d.	n.d.
939	48644	-1.58	0.901	25.9	n.d.	n.d.	n.d.
943	48956	-1.32	0.898	25.8	n.d.	n.d.	14.06
945	49111	-1.27	n.d.	n.d.	n.d.	n.d.	n.d.
949	49422	-1.66	0.896	25.7	n.d.	n.d.	n.d.
953	49733	-1.67	0.891	25.4	n.d.	n.d.	13.79
955	49889	-1.51	n.d.	n.d.	n.d.	n.d.	n.d.
959	50200	-1.91	0.902	26.0	n.d.	n.d.	12.26
963	50511	-1.54	0.908	26.3	n.d.	n.d.	n.d.
965	50667	-1.96	n.d.	n.d.	n.d.	n.d.	n.d.
969	50978	-1.99	0.908	26.3	n.d.	n.d.	n.d.
973	51289	-1.69	0.907	26.3	n.d.	n.d.	14.63

975	51444	-1.82	n.d.	n.d.	n.d.	n.d.	n.d.
979	51756	-1.90	0.907	26.3	3.57	26.9	15.15
984	52144	-2.06	0.906	26.2	3.40	26.4	10.32
989	52533	-2.15	0.903	26.1	n.d.	n.d.	n.d.
993	52844	-1.97	0.904	26.1	3.84	27.7	9.00
995	53000	-2.00	n.d.	n.d.	n.d.	n.d.	n.d.
999	53333	-1.89	0.902	26.0	n.d.	n.d.	n.d.
1003	53667	-1.65	0.902	26.0	n.d.	n.d.	8.56
1005	53833	-1.62	n.d.	n.d.	n.d.	n.d.	n.d.
1009	54167	-1.73	0.902	26.0	n.d.	n.d.	n.d.
1013	54500	-1.43	0.905	26.2	3.43	26.5	10.19
1015	54667	-1.58	n.d.	n.d.	n.d.	n.d.	n.d.
1019	55000	-1.82	0.913	26.6	n.d.	n.d.	n.d.
1023	55333	-1.54	0.911	26.5	n.d.	n.d.	9.35
1025	55500	-1.31	n.d.	n.d.	n.d.	n.d.	n.d.
1029	55833	-0.91	0.916	26.7	n.d.	n.d.	n.d.
1033	56167	-1.62	0.917	26.8	n.d.	n.d.	9.41
1035	56333	-1.87	n.d.	n.d.	n.d.	n.d.	n.d.
1039	56667	-1.74	0.928	27.4	n.d.	n.d.	n.d.
1043	57000	-1.54	0.926	27.3	n.d.	n.d.	11.55
1045	57167	-1.79	n.d.	n.d.	n.d.	n.d.	n.d.
1049	57500	-1.86	0.925	27.2	n.d.	n.d.	n.d.
1051	57667	-1.78	n.d.	n.d.	n.d.	n.d.	n.d.
1053	57833	-0.83	0.927	27.3	3.56	26.9	8.35
1055	58000	-0.80	n.d.	n.d.	n.d.	n.d.	n.d.
1059	58269	-1.06	0.923	27.1	n.d.	n.d.	n.d.
1063	58538	-1.36	0.915	26.7	3.72	27.4	13.18
1065	58672	-0.84	n.d.	n.d.	n.d.	n.d.	n.d.
1069	58941	-0.75	0.912	26.5	n.d.	n.d.	n.d.
1073	59210	-0.77	0.913	26.6	3.81	27.6	16.41
1075	59345	-0.59	n.d.	n.d.	n.d.	n.d.	n.d.
1079	59613	-0.95	0.909	26.4	n.d.	n.d.	n.d.
1083	59882	-0.59	0.907	26.3	3.48	26.6	13.62
1085	60017	-1.09	n.d.	n.d.	n.d.	n.d.	n.d.
1089	60286	-1.10	0.894	25.6	n.d.	n.d.	n.d.
1093	60555	-0.75	0.905	26.2	n.d.	n.d.	n.d.
1095	60689	-0.66	n.d.	n.d.	n.d.	n.d.	n.d.
1099	60958	-1.25	0.903	26.1	n.d.	n.d.	n.d.
1103	61227	-1.31	0.907	26.3	n.d.	n.d.	n.d.
1105	61361	-1.17	n.d.	n.d.	n.d.	n.d.	n.d.
1109	61630	-1.34	0.908	26.3	n.d.	n.d.	n.d.
1113	61899	-1.32	0.909	26.4	n.d.	n.d.	n.d.
1115	62034	-1.23	n.d.	n.d.	n.d.	n.d.	n.d.
1119	62303	-1.86	0.909	26.4	n.d.	n.d.	n.d.
1123	62571	-1.68	0.911	26.5	n.d.	n.d.	n.d.
1125	62706	-1.54	n.d.	n.d.	n.d.	n.d.	n.d.
1127	62840	n.d.	0.91	26.4	n.d.	n.d.	n.d.
1128	62908	-1.75	0.906	26.2	n.d.	n.d.	n.d.
1130	63042	n.d.	0.911	26.5	n.d.	n.d.	n.d.
1134	63311	-1.44	n.d.	n.d.	n.d.	n.d.	n.d.
1137	63513	-1.22	0.908	26.3	n.d.	n.d.	n.d.
1140	63714	n.d.	0.899	25.8	n.d.	n.d.	n.d.
1144	63983	-0.99	0.906	26.2	n.d.	n.d.	n.d.
1149	64319	n.d.	0.908	26.3	n.d.	n.d.	n.d.
1151	64454	-1.70	0.903	26.1	n.d.	n.d.	n.d.
1160	65059	n.d.	0.911	26.5	n.d.	n.d.	n.d.
1164	65328	n.d.	0.893	25.5	n.d.	n.d.	n.d.
1165	65395	n.d.	0.905	26.2	n.d.	n.d.	n.d.

1169	65664	-1.30	n.d.	n.d.	n.d.	n.d.	n.d.
1174	66000	-1.63	0.891	25.4	n.d.	n.d.	n.d.
1180	66603	-1.26	0.906	26.2	n.d.	n.d.	n.d.
1184	67005	-1.49	0.896	25.7	n.d.	n.d.	n.d.
1190	67608	-1.66	0.908	26.3	n.d.	n.d.	n.d.
1194	68010	-1.28	0.909	26.4	n.d.	n.d.	n.d.
1200	68612	-1.64	0.9	25.9	n.d.	n.d.	n.d.
1204	69014	-1.81	0.912	26.5	n.d.	n.d.	n.d.
1210	69617	n.d.	0.908	26.3	n.d.	n.d.	n.d.
1214	70019	-1.85	0.912	26.5	n.d.	n.d.	n.d.
1220	70622	n.d.	0.919	26.9	n.d.	n.d.	n.d.
1224	71024	-1.65	0.903	26.1	n.d.	n.d.	n.d.
1230	71627	n.d.	0.89	25.4	n.d.	n.d.	n.d.
1234	72029	n.d.	0.896	25.7	n.d.	n.d.	n.d.
1240	72632	-1.79	0.914	26.6	n.d.	n.d.	n.d.
1244	73033	-0.88	0.907	26.3	n.d.	n.d.	n.d.
1250	73636	n.d.	0.909	26.4	n.d.	n.d.	n.d.
1254	74038	-1.71	0.917	26.8	n.d.	n.d.	n.d.
1260	74641	n.d.	0.917	26.8	n.d.	n.d.	n.d.
1264	75043	-1.85	0.909	26.4	n.d.	n.d.	n.d.
1270	75646	n.d.	0.916	26.7	n.d.	n.d.	n.d.
1275	76148	-1.60	0.917	26.8	n.d.	n.d.	n.d.
1279	76550	-1.76	n.d.	n.d.	n.d.	n.d.	n.d.
1283	76952	n.d.	0.92	26.9	n.d.	n.d.	n.d.
1289	77555	-2.35	n.d.	n.d.	n.d.	n.d.	n.d.
1293	77957	-1.57	0.92	26.9	n.d.	n.d.	n.d.
1299	78560	-2.08	n.d.	n.d.	n.d.	n.d.	n.d.
1303	78962	-1.66	0.914	26.6	n.d.	n.d.	n.d.
1309	79565	-1.79	n.d.	n.d.	n.d.	n.d.	n.d.
1313	79967	-1.47	0.912	26.5	n.d.	n.d.	n.d.
1323	80971	-1.70	0.918	26.8	n.d.	n.d.	n.d.
1329	81574	-1.75	n.d.	n.d.	n.d.	n.d.	n.d.
1334	82077	-1.95	0.918	26.8	n.d.	n.d.	n.d.
1339	82579	-1.62	n.d.	n.d.	n.d.	n.d.	n.d.
1343	82981	-1.87	0.921	27.0	n.d.	n.d.	n.d.
1349	83584	-1.43	n.d.	n.d.	n.d.	n.d.	n.d.
1353	83986	-1.76	0.941	28.1	n.d.	n.d.	n.d.
1359	84589	-2.15	n.d.	n.d.	n.d.	n.d.	n.d.
1363	84990	-1.19	0.935	27.7	n.d.	n.d.	n.d.
1369	85593	-1.29	n.d.	n.d.	n.d.	n.d.	n.d.
1373	85995	-1.41	0.925	27.2	n.d.	n.d.	n.d.
1379	86598	-2.11	n.d.	n.d.	n.d.	n.d.	n.d.
1383	87000	-1.71	0.929	27.4	n.d.	n.d.	n.d.
1389	87700	-1.33	n.d.	n.d.	n.d.	n.d.	n.d.
1393	88167	-1.87	0.921	27.0	n.d.	n.d.	n.d.
1403	89334	n.d.	0.945	28.3	n.d.	n.d.	n.d.

radiocarbon data			
depth in core MD02-2529 (cm)	**corrected depth (cm)**	**14C age (yr BP)**	**uncertainty**
8-16 *N. dutertrei*	12	870	45
135-137 *N. dutertrei*	136	3480	80
246-247 *N. dutertrei*	359.5	10140	70
294-295 *N. dutertrei*	407.5	11920	90
294-295 *G. ruber*	407.5	11670	100
356-357 *N. dutertrei*	469.5	14080	100
356-357 *G. ruber*	469.5	14260	140
357-358 *N. dutertrei*	470.5	14530	110
357-358 *G. ruber*	470.5	14440	110
404-406 *N. dutertrei*	518	16620	130
404-406 *G. ruber*	518	16730	140
477-478 *N. dutertrei*	590.5	20470	130
566-568 *N. dutertrei*	680	25970	240
575-576 *N. dutertrei*	688.5	26580	260
707-708 *N. dutertrei*	790.5	34260	650

age model for MD02-2529			
corrected depth (cm)	**cal. Age (yr BP)**	**uncert 2□**	**notes**
12	446	120	MARINE04
136	3287	244	MARINE04
359.5	11004	231.5	MARINE04
407.5	13344	208.5	MARINE04
470	16508	443	MARINE04, average of 469-471 cm depth
518	19277	266.5	MARINE04
590.5	23974	384.5	MARINE04
680	30320		poly Bard 04 (on GISP2 timescale)
688.5	30961		poly Bard 04 (on GISP2 timescale)
790.5	38639		poly Bard 04 (on GISP2 timescale)
905	46000		tuned to Byrd (on GISP2 timescale)
995	53000		tuned to Byrd (on GISP2 timescale)
1055	58000		tuned to Byrd (on GISP2 timescale)
1174	66000		tuned to benthic $\delta^{18}O$ stack
1383	87000		tuned to benthic $\delta^{18}O$ stack

Table 2: Radiocarbon age results of MD02-2529 core and their corresponding calibrated calendar ages (upper panel, see SI3 for details of calculation). Age model for MD02-2529 (lower panel). The corresponding references of the Table 2 in the "notes" column are: [S32] for MARINE04, [S34] for the polynomial calculation of radiocarbon ages beyond 25,000 ^{14}C yr BP, [S35] for the GISP2 timescale, [S40] for the benthic $\delta^{18}O$ stack and [S38] for Byrd.

References :

S1. Fiedler, P. C. The annual cycle and biological effects of the Costa Rica Dome. *Deep Sea Res. Part I* **49**, 321-338 (2002).

S2. Magaña, V., Amador, J. A. & Medina, S. The Midsummer Drought over Mexico and Central America. *J. Clim.* **12**, 1577-1588 (1999).

S3. Rodriguez-Rubio, E., Schneider, W. & Abarca del Rio, R. On the seasonal circulation within the Panama Bight derived from satellite observations of wind, altimetry and sea surface temperature. *Geophys. Res. Lett.* **30**, 1410, doi:10.1029/2002GL016794 (2003).

S4. Linsley, B. K., Dunbar, R. B., Wellington, G. M. & Mucciarone, D. A. A coral-based reconstruction of Intertropical Convergence Zone variability over Central America since 1707. *J. Geophys. Res.* **99**, 9977-9994 (1994).

S5. Liu, W. T. & Tang, W. Estimating moisture transport over oceans using space-based observations. *J. Geophys. Res.* **110**, D10101, doi:10.1029/2004JD005300 (2005).

S6. Poveda, G., Waylen, P. R. & Pulwarty, R. S. Annual and inter-annual variability of the present climate in northern South America and southern Mesoamerica, *Palaeogeogr. Palaeoclimatol. Palaeoecol.* **234**, 3-27 (2006).

S7. Benway, H. M. & Mix, A. C. Oxygen isotopes, upper-ocean salinity, and precipitation sources in the eastern tropical Pacific. *Earth Planet. Sci. Let.* **224**, 493-507 (2004).

S8. Mix, A. C., Morey, A. E., Pisias, N. G. & S. W. Hostetler. Foraminiferal faunal estimates of paleotemperature: Circumventing the no-analog problem yields cool ice ages tropics, *Paleoceanography*, **14(3)**, 350, doi:10.1029/1999PA900012 (1999).

S9. Benway, H. M., Mix, A. C., Haley, B. A. & Klinkhammer, G. P. Eastern Pacific Warm Pool paleosalinity and climate variability: 0-30 kyr. *Paleoceanography* **21**, PA3008, doi:10.1029/2005PA001208 (2006).

S10. Fairbanks, R. G., Sverdlove, M., Free, R., Wiebe, P. & Bé, W. H. Vertical distribution and isotopic fraction of living planktonic foraminifera from the Panama Basin. *Nature*, **298**, 841-844 (1982).

S11. Kroopnick, P. The dissolved O_2-CO_2-^{13}C system in the eastern equatorial pacific. *Deep-Sea Res.*, **21(3)**, 211-227 (1974).

S12. Sonzogni, C., *et al.* Temperature and salinity effects on alkenone ratios measured in surface sediments from the Indian Ocean. *Quat. Res.* **47**, 344-355 (1997).

S13. Rosell-Melé, A. *et al*. Precision of the current methods to measure the alkenone proxy $U_{37}^{k'}$ and absolute alkenone abundance in sediments: Results of an interlaboratory comparison study. *Geochem. Geophys. Geosyst.* **2**, doi: 10.1029/2000GC000141 (2001).

S14. Müller, P. J., Kirst, G., Ruhland, G., von Storch, I. & Rosell-Melé, A. Calibration of the alkenone paleotemperature index $U_{37}^{k'}$ based on core tops from the eastern South Atlantic and the global ocean (60°N-60°S). *Geochim. et Cosmochim. Acta* **62**, 1757-1772 (1998).

S15. Conte, M. H., Thompson, A., Lesley, D. & Harris, R. P. Genetic and physiological influences on the alkenone/alkenoate versus growth temperature relationship in *Emiliania huxleyi* and *Gephyrocapsa oceanica*. *Geochim. et Cosmochim. Acta* **62**, 51-68 (1998).

S16. Conte, M. H., Weber, J. C., King, L. L. & Wakeham, S. G. The alkenone temperature signal in western North Atlantic surface waters. *Geochim. et Cosmochim. Acta* **65**, 4275-4287 (2001).

S17. Conte, M. H., *et al*. Global temperature calibration of the alkenone unsaturation index ($U_{37}^{k'}$) in surface waters and comparison with surface sediments. *Geochem. Geophys. Geosyst.* **7**, Q02005 doi: 10.1029/2005GC001054 (2006).

S18. Boyle, E. A. & Keigwin, L. D. Comparison of Atlantic and Pacific paleochemical records for the last 215,000 years: changes in deep ocean circulation and chemical inventories. *Earth Planet. Sci. Let.* **76**, 135-150 (1985/86).

S19. Boyle, E. A. & Rosenthal, Y. Chemical hydrography of the South Atlantic during the Last Glacial Maximum: $\delta^{13}C$ vs. Cd, pp. 423-443 in: Wefer, G. et al., (eds) The South Atlantic: present and past circulation. (Springer-Verlag, Berlin, 1996).

S20. Pena, L. D., Calvo, E., Cacho, I., Eggins, S. & Pelejero, C. Identification of Mn-Mg-rich contaminant phases on foraminiferal tests: Implications for Mg/Ca past temperature reconstructions. *Geochem. Geophys. Geosyst.* **6**, Q09P02 doi: 10.1029/2005GC000930 (2005).

S21. Rosenthal, Y. et al. Interlaboratory comparison study of Mg/Ca and Sr/Ca measurements in planktonic foraminifera for paleoceanographic research. *Geochem. Geophys. Geosyst.* **5**, Q04D09 doi: 10.1029/2003GC000650 (2004).

S22. Lea, D. W., Pak, D. K. & Spero, H. J. Climate impact of Late Quaternary Equatorial Pacific sea surface temperature variations. *Science* **289**, 1719-1724 (2000).

S23. Bard, E. Paleoceanographic implications of the difference in deep-sea sediment mixing between large and fine particles. *Paleoceanography* **16**, 235-239, (2001).

S24. Thunell, R. C., Curry, W. B. & Honjo, S. Seasonal variation in the flux of planktonic foraminifera: time series sediment trap results from the Panama Basin. *Earth Planet. Sci. Let.* **64**, 44-55 (1983).

S25. Bemis, B. E., Spero, H. J., Bijma, J. & Lea, D. W. Reevaluation of the oxygen isotopic composition of planktonic foraminifera: Experimental results and revised paleotemperature equations. *Paleoceanography* **13**, 150-160 (1998).

S26. Waelbroeck, C., *et al.* Sea-level and deep water temperature changes derived from benthic foraminifera isotopic records. *Quat. Sci. Rev.* **21**, 295-305 (2002).

S27. Siddall, M., *et al.* Sea-level fluctuations during the last glacial cycle. *Nature* **423**, 853-858 (2003).

S28. Shackleton, N. J., Hall, M. A. & Vincent, E. Phase relationships between millennial-scale events 64,000-24,000 years ago. *Paleoceanography* **15**, 565-569 (2000).

S29. Duplessy J.C., Bard E., Arnold M., Shackleton N.J., Duprat J. & Labeyrie L.D.. How fast did the ocean-atmosphere system run during the last deglaciation. *Earth Planet. Sci. Lett.* **103**, 27-40, (1991).

S30. Schmidt, G. A. Error analysis of paleosalinity calculation. *Paleoceanography* **14**, 422-429 (1999).

S31. WOCE, World Ocean Circulation Experiment. Data available at http://woce.nodc.noaa.gov/wdiu/updates/

S32. Hughen, K. A., *et al.*, MARINE04 marine Radiocarbon age calibration, 26-0 ka BP. *Radiocarbon* **46**, 1059-1086 (2004).

S33. Stuiver, M., Reimer, P. J. & Reimer, R. CALIB Radiocarbon Calibration software, available online at http://calib.qub.ac.uk/calib/

S34. Bard, E., Rostek, F. & Ménot-Combes, G. Radiocarbon calibration beyond 20,000 ^{14}C yr B.P. by means of planktonic foraminifera of the Iberian Margin. *Quat. Res.* **61**, 204-214 (2004).

S35. Stuiver, M. & Grootes, P. M. GISP2 oxygen isotope ratios. *Quat. Res.* **53**, 277-284 (2000).

S36. Pahnke, K. & Zahn, R. Southern Hemisphere water mass conversion linked with North Atlantic climate variability. *Science* **307**, 1741-1746 (2005).

S37. Martin, P., Archer, D. & Lea, D. W. Role of deep sea temperature on the carbon cycle during the last glacial. *Paleoceanography* **20**, PA2015 doi: 10.1029/2003PA000914 (2005).

S38. Brook, E. J., *et al.* Timing of millennial-scale climate change at Siple Dome, West Antarctica, during the last glacial period. *Quat. Sci. Rev.* **24**, 1333-1343 (2005).

S39. Peterson, L. C., Haug, G. H., Hughen, K. A. & Röhl, U. Rapid changes in the hydrologic cycle of the tropical Atlantic during the Last Glacial. *Science* **290**, 1947-1951 (2000).

S40. Lisiecki, L. E. & Raymo, M. E. A Pliocene-Pleistocene stack of 57 globally distributed benthic $\delta^{18}O$ records. *Paleoceanography* **20**, PA1003 doi: 10.1029/2004PA001071 (2005).

S41. Conkright, M. E. *et al*. World Ocean Atlas 2001: Objective Analyses, Data Statistics, and Figures, CD-ROM Documentation. National Oceanographic Data Center, Silver Spring, MD, 17 pp (2002). Data available at: http://ingrid.ldeo.columbia.edu

S42. DaSilva, A., Young, A. C. & Levitus, S. Atlas of Surface Marine Data (1994), Volume 1: Algorithms and Procedures. NOAA Atlas NESDIS 6, U.S. Department of Commerce, Washington, D.C., 1994. Data available at http://ingrid.ldeo.columbia.edu

S43. O'Neil, J. R., Clayton, R. N. & Mayeda, T. K. Oxygen isotope fractionation in divalent metal carbonates. *J. Chem. Phys*. **51**, 5547-5558 (1969).

S44. Curry, W. B., Thunell, R. C. & Honjo, S. Seasonal changes in the isotopic composition of planktonic foraminifera collected in Panama Basin sediment traps. *Earth Planet. Sci. Let*. **64**, 33-43 (1983).

S45. Spero, H. J., Mielke, K. M., Kalve, E. M., Lea, D. W. & Pak, D. K. Multispecies approach to reconstructing eastern equatorial Pacific thermocline hydrography during the past 360 kyr. *Paleoceanography* **18**, 1022, doi:10.1029/2002PA000814 (2003).

S46. Schmidt, M. W., Spero, H. J. & Lea, D. W. Links between salinity variation in the Caribbean and North Atlantic thermohaline circulation. *Nature* **428**, 160-163 (2004).